https://doi.org/10.5194/egusphere-2026-1856
Preprint. Discussion started: 10 April 2026

Incorporating irrigation effects into high-resolution daily land evaporation estimates over the Iberian Peninsula

Oscar M. Baez-Villanueva[1], Alfredo Crespo-Otero[2], Sara Modanesi[3,4], Pierre Laluet[5], Sergio Vicente-Serrano[6,7], Jaap Schellekens[8], Jacopo Dari[9,3], Hylke E. Beck[10], Wouter Dorigo[5], Christian Massari[3], Chiara Corbari[11], Joppe Massant[1], Kwint Delbare[1], Olivier Bonte[1], Aaron Boone[12], Diego Fernández-Prieto[13], and Diego G. Miralles[1]

[1]Hydro-Climate Extremes Lab (H-CEL), Ghent University, Belgium
[2]CRETUS, Nonlinear Physics Group, Universidade de Santiago de Compostela, Santiago de Compostela, Spain
[3]Research Institute for Geo-Hydrological Protection, National Research Council, Perugia, Italy
[4]Department of Earth and Environmental Sciences, KU Leuven, Heverlee, Belgium
[5]Department of Geodesy and Geoinformation, TU Wien, Vienna, Austria
[6]Instituto Pirenaico de Ecología, Consejo Superior de Investigaciones Científicas (IPE- CSIC), Zaragoza, Spain
[7]Laboratorio de Climatología y Servicios Climáticos (LCSC), CSIC-University of Zaragoza, Zaragoza, Spain
[8]Stichting Deltares, Delft, Netherlands
[9]Department of Civil and Environmental Engineering, University of Perugia, Perugia, Italy
[10]King Abdullah University of Science and Technology (KAUST), Thuwal, Saudi Arabia
[11]Department of Civil and Environmental Engineering, Politecnico di Milano, Milan, Italy
[12]Météo-France, CNRS, Université de Toulouse, CNRM, Toulouse, France
[13]European Space Agency, ESA-ESRIN, Largo Galileo Galilei, Frascati, Italy

Correspondence: Oscar M. Baez-Villanueva (Oscar.BaezVillanueva@ugent.be)

Abstract. Land evaporation (E) links the water, energy, and carbon cycles and plays a central role in agriculture, water management, and land–climate interactions. However, estimating E at high spatial and temporal resolution remains challenging, especially in irrigated regions. This study presents a novel framework to generate daily 1 km E estimates for 2018–2022 over the Iberian Peninsula by explicitly representing irrigation in the recently released Global Land Evaporation Amsterdam Model version 4 (GLEAM4). To this end, high-resolution (1 km) meteorological forcing is combined with Sentinel-1 soil moisture and ancillary information on irrigated extent and satellite-based crop phenology. Our method constrains E below potential evaporation (E_p) even in irrigated land, leveraging observational data of vapour pressure deficit, air temperature, vegetation optical depth, leaf area index, wind speed, and shortwave radiation, which allows irrigated crops to respond realistically to diverse sources of vegetation stress, rather than assuming E_p rates. Results reveal increases in E over irrigated areas of up to 450 mm yr^{-1} when irrigation is explicitly considered, with spatial patterns consistent with independent irrigation estimates. Evaluation against eddy-covariance measurements demonstrates marked improvements at two irrigated sites in the Iberian Peninsula, with increases in daily Kling-Gupta Efficiency (KGE) compared to simulations without irrigation of 0.40 and 0.70, respectively. The approach is also relatively robust to false positives in the irrigation mask owing to the fractional vegetation structure of GLEAM4. Overall, the resulting high-resolution E dataset provides a realistic representation of irrigation practices and supports applications in both agricultural management and regional water-resource assessments. The approach will be extended to global scales through integration into future GLEAM releases.

https://doi.org/10.5194/egusphere-2026-1856
Preprint. Discussion started: 10 April 2026

1 Introduction

Land evaporation (or *'evapotranspiration'*, E) is a key variable at the interface of agriculture, water management, and climate. It links the energy, water, and carbon cycles (Tran et al., 2023; Fisher et al., 2017; Liu et al., 2015), and strongly influences water availability and ecosystem health (Zhao et al., 2022). Despite its central role, hydrological research has traditionally focused on the supply and storage side of the water balance (precipitation, runoff, soil moisture, and groundwater) while the demand side, largely controlled by E, has received comparatively less attention (Fisher et al., 2017). In many regions, evaporative demand and anthropogenic pressure on water resources are increasing simultaneously (Scanlon et al., 2023), contributing to more frequent and intense drought events (Gebrechorkos et al., 2025). Accurate quantification of E is therefore critical, particularly in agricultural systems where it governs crop productivity, determines irrigation requirements, and modulates water-use efficiency (Gong et al., 2024; Junquera et al., 2025).

Irrigated agriculture is one of the largest consumptive uses of freshwater globally (Massari et al., 2021), yet its contribution to total water withdrawals remains highly uncertain and site-dependent, with estimates ranging between 45% and 90% (Puy et al., 2025). In irrigated systems, E reflects not only natural processes but also human management decisions, as irrigation increases soil moisture availability, modifies surface energy fluxes, and can influence local to regional climate through feedbacks on temperature and humidity (Han et al., 2014; McDermid et al., 2023). At the same time, the overexploitation of surface and groundwater resources has led to substantial declines in water storage in many regions, particularly in semi-arid and arid environments where irrigation sustains agricultural production during periods of high evaporative demand (Gong et al., 2024). These factors highlight the importance of explicitly representing irrigation in E models, even those dedicated to large, climatological scales. However, accurately characterising the timing and spatial distribution of irrigation remains challenging due to limited ground-based observations, incomplete reporting of water withdrawals, and inconsistencies among remote-sensing products and methodologies, which lead to uncertainties in both irrigation extent and applied volumes (Dari et al., 2023; McDermid et al., 2023; Zappa et al., 2024; Laluet et al., 2025, 2026).

Early remote sensing-based E models were primarily based on surface energy balance approaches combining temperature and vegetation information, such as the Surface Energy Balance Algorithm for Land (SEBAL; Bastiaanssen et al., 1998), the Satellite-Based Energy Balance for Mapping Evapotranspiration with Internalized Calibration (METRIC; Allen et al., 2007), the Atmosphere Land Exchange Inverse (ALEXI; Anderson et al., 1997), and the Two-Source Energy Balance (TSEB; Norman et al., 1995; Kustas et al., 2004). These models can be applied at high spatial resolutions and reflect irrigation influences on land surface temperature, but they typically provide instantaneous or discontinuous snapshots of E and are not designed for continuous application at continental to global scales. Two clear examples are (i) the successful Open-ET initiative (Melton et al., 2022), which currently provides data over the conterminous United States with a goal latency of six weeks at 30 m spatial resolution (OpenET, 2026); and (ii) the CMRSET dataset (Guerschman et al., 2022), which provides monthly E data at a 30 m resolution over Australia. While these frameworks are well suited to field- or basin-scale applications, their reliance on instantaneous satellite overpasses limits their ability to produce temporally continuous records required for climate and hydrological studies.

https://doi.org/10.5194/egusphere-2026-1856
Preprint. Discussion started: 10 April 2026

In contrast, E models developed for climate applications prioritise temporal continuity and global consistency (Miralles et al., 2016; McCabe et al., 2016). Penman–Monteith-based global products such as MOD16 (Endsley et al., 2025; Mu et al., 2011) and the Penman-Monteith-Leuning Evapotranspiration (PML; Zhang et al., 2019), as well as Priestley and Taylor-based approaches like the Priestley and Taylor Jet Propulsion Laboratory (PT-JPL; Fisher et al., 2008), or previous versions of the Global Land Evaporation Amsterdam Model (GLEAM; Miralles et al., 2011), have the advantage of being continuous and coherent over large spatio-temporal scales. The same is true for machine-learning-based approaches dedicated to large-scale E estimation (Jung et al., 2009; Nelson et al., 2024). However, the coarser spatial resolution of these climate datasets (around 0.1–0.25°) limits their ability to represent local heterogeneity and to inform basin- or regional-scale water management and agricultural decisions. Moreover, most global E products do not explicitly represent irrigation, implicitly assuming that water availability is determined by natural precipitation and soil moisture dynamics. Recent methodological advances aim to bridge this gap by targeting higher spatial resolutions while maintaining physical consistency, scalability, and the capacity to generate long-term records that capture fine-scale heterogeneity and human influences over large scales (Yi et al., 2024). For example, the FAO's Water Productivity through Open access of Remotely sensed derived data evaporation dataset (WaPOR v3.0; FAO, 2020) has been explicitly designed for agricultural applications and offers global data at a 10-day temporal resolution; likewise, PT-JPL, even though it was not originally designed for agriculture, provides estimates at high resolution as part of the Open ET ensemble (Melton et al., 2022).

GLEAM (GLEAM; Miralles et al., 2011) was originally developed to generate global, coarse resolution, long-term records of E based on a process-based framework driven by satellite data. While its applicability at higher spatial resolutions has already been demonstrated (Martens et al., 2018), GLEAM has not been explicitly designed or evaluated for its ability to represent E dynamics in irrigated land. As GLEAM transitions to target increasingly higher spatial resolutions and broader applications in water management and agriculture, there is a clear need to extend the framework to explicitly represent irrigation practices. Approaches that combine physical modelling with data assimilation offer a promising pathway forward. For example, Modanesi et al. (2025) optimised a sprinkler irrigation scheme within a land surface model using Sentinel-1–based irrigation estimates. Similarly, Van Dijk et al. (2018) assimilated thermal satellite observations into a global hydrological model to improve E estimates by accounting for E from surface and groundwater resources, while combining this framework with a simple irrigation water balance model to estimate minimum irrigation requirements globally. While GLEAM already assimilates coarse resolution surface soil moisture observations, its ability to represent irrigation is still hampered by the low resolution and the lack of explicit parametrisation over irrigated landscapes. Consequently, irrigation effects are only indirectly represented through soil moisture and vegetation signals and cannot be resolved reliably at field to regional scales.

This study addresses that need by developing and evaluating a strategy to estimate daily E at high spatial resolution (1 km), while explicitly incorporating the contribution of irrigation into the most recent version of GLEAM (GLEAM4; Miralles et al., 2025). Our approach combines high-resolution meteorological forcing, satellite soil moisture estimates, and information on irrigated extent and crop phenology to constrain irrigation-driven E within the GLEAM framework. Specifically, we aim to: (i) derive daily E estimates at 1 km spatial resolution for 2018–2022 over the Iberian Peninsula by forcing GLEAM4 with high-resolution meteorological inputs; (ii) integrate the contribution of irrigation to E into the GLEAM4 framework in a way

https://doi.org/10.5194/egusphere-2026-1856
Preprint. Discussion started: 10 April 2026

that accounts for diverse environmental stressors beyond water availability; (iii) evaluate the model's ability to capture E dynamics, including those influenced by irrigation practices; and (iv) assess the implications of explicitly representing irrigation for the spatial and temporal patterns of E across the Iberian Peninsula. The approach is designed as a pilot implementation that can be scaled and extended to global production and to other E models and datasets. Since accounting for irrigation is particularly critical in semiarid regions such as the Mediterranean basin, the Iberian Peninsula is selected as a testbed. The strong gradients in precipitation and temperature, complex topography, and extensive irrigated areas characterised by pronounced seasonality in both water and energy availability, make the region an ideal test case for assessing the added value of explicitly representing irrigation in GLEAM. A key novelty of this study is that irrigation effects are integrated while allowing E to be constrained below potential evaporation (E_p) by multiple environmental variables that modulate vegetation stress and stomatal conductance. The approach provides a physically consistent representation of how irrigation interacts with the broader biophysical environment without assuming that irrigated areas evaporate at potential rates, and can be fully driven by satellite data at the global scale.

2 Study area

The study area, spanning mainland Spain, and Portugal, is shown in Figure 1, and is hereafter referred to as the Iberian Peninsula. The peninsula covers an area of approximately 580,000 km^2 and features large precipitation and temperature gradients, complex topography, and heterogeneous land use patterns that shape contrasting hydroclimatic conditions (Carvalho et al., 2021). Elevations range from sea level along the Atlantic and Mediterranean coasts to over 3,400 m a.s.l. in the Pyrenees and Sierra Nevada mountains. The climate of the Iberian Peninsula is characterised by pronounced spatial and seasonal variability. Atlantic-influenced regions in the north-west receive over 2,000 mm of precipitation, while semi-arid and arid zones in the south-east receive less than 100 mm year^{-1} (Alvarez et al., 2025; Ilvonen et al., 2022; Serrano-Notivoli et al., 2018). The Mediterranean region and the continental central plateau face strong seasonal contrasts between wet winters and hot, dry summers, being vulnerable to water scarcity and drought. Moreover, climate projections suggest that drought events in the region are likely to become more severe and frequent in the future (Jézéquel et al., 2025; Lazoglou et al., 2024; Lorenzo et al., 2024; García-Valdecasas Ojeda et al., 2021; Ojeda et al., 2021; Spinoni et al., 2020).

Agriculture is the key economic sector across much of the peninsula, encompassing diverse agroforestry and mixed-cropping systems characteristic of Mediterranean agriculture (Cruz Maceín et al., 2023). Irrigated croplands are concentrated in the Ebro, Guadalquivir, and Tagus River basins, as well as the Mediterranean coastal plains. Irrigated lands in Spain have expanded from 1.5 to nearly 4 million hectares since 1950, reflecting a general intensification over recent decades (Beguería et al., 2022; Duarte et al., 2014). The Ebro Basin, in northeastern Spain, is one of the most intensively irrigated areas of southern Europe, consuming high amounts of water (Funes et al., 2021), and supporting a wide variety of crops such as maize, alfalfa, barley, wheat, olives, grapes, and fruit trees (Dari et al., 2024a; Pinilla, 2006). Irrigation practices in these areas are sustained through an extensive system of dams and canals that regulate water flow and storage (Sutanto et al., 2024).

https://doi.org/10.5194/egusphere-2026-1856
Preprint. Discussion started: 10 April 2026

Land cover across the Iberian Peninsula is dominated by agricultural lands and forests; croplands and pastures are prevalent in lowlands and forested ecosystems dominate mountain ranges (Figure 1b). Eight eddy-covariance sites are located within the Iberian Peninsula and are also shown in Figure 1. Of these sites, two are irrigated and six are non-irrigated, representing contrasting water management conditions. A detailed description of their temporal data availability, irrigation practices, and general characteristics is provided in Table 1.

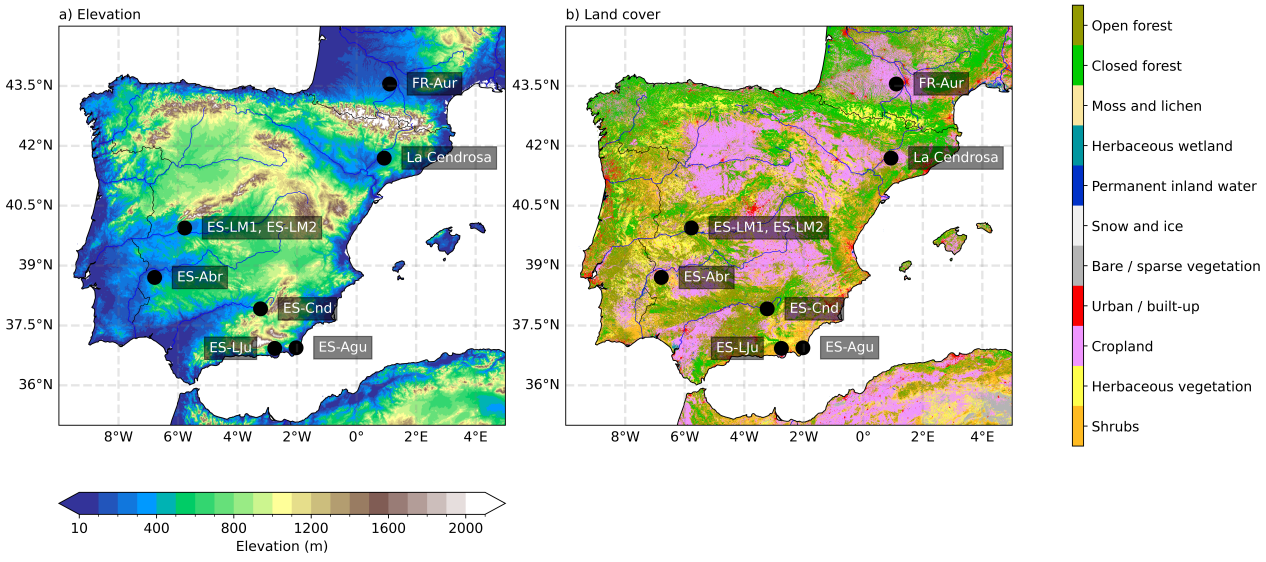

Figure 1. The Iberian Peninsula showing (a) elevation from the ETOPO Global Relief Model (NOAA, 2022), and (b) land cover from the CORINE Land Cover dataset (Bossard et al., 2000). Eddy-covariance stations are shown as black dots. For a detailed description of the sites, see Table 1.

3 Data and methods

To produce a daily high-resolution E dataset for 2018–2022 that explicitly accounts for the contribution of irrigation, we use GLEAM4 (Miralles et al., 2025) and adopt a four-step procedure consisting of: (i) generating a 1 km forcing dataset for the analysis period over the Iberian Peninsula; (ii) developing a strategy to explicitly represent irrigation in space and time within GLEAM4; (iii) executing GLEAM4 at high resolution with two configurations, one including and one excluding irrigation (benchmark); and (iv) evaluating the performance of the resulting E estimates. These steps are described below and summarised in Figure 2a.

3.1 GLEAM4 baseline

GLEAM4 (Miralles et al., 2025) is a hybrid model that combines process-based knowledge with AI-driven techniques to enhance E and soil moisture estimates over varying climatic conditions. It focuses on key processes that directly impact E by

https://doi.org/10.5194/egusphere-2026-1856
Preprint. Discussion started: 10 April 2026

Table 1. Overview of the selected eddy-covariance sites used in this study, including location, climate characteristics, and data availability within the simulation period (2018–2022).

Site	Data availability	Irrigated	Description
Albuera (ES-Abr)	2018–2020	No	Savannas (herbaceous and other understory systems with forest canopy cover of evergreen holm oaks between 10–30%).
Majadas del Tiétar North (ES-LM1)	2018–2020	No	Savannas (herbaceous and other understory systems with forest canopy cover between 10–30%).
Majadas del Tiétar South (ES-LM2)	2018–2020	No	Savannas (herbaceous and other understory systems with forest canopy cover between 10–30%).
Aguamarga (ES-Agu)	2018–2020	No	Open shrublands (woody vegetation less than 2 m tall and with shrub canopy cover between 10–60%).
Llano de los Juanes (ES-LJu)	2018–2020	No	Open shrublands (woody vegetation less than 2 m tall and with shrub canopy cover between 10–60%).
La Cendrosa (Ebro)	2021	Yes	Irrigated alfalfa with multiple harvests in the growing season. Irrigation through flood or gravity methods (Boone et al., 2025).
Conde (ES-Cnd)	2018–2020	Yes	Woody savanna site with irrigated olives.
Aurade (FR-Aur)	2018–2022	No	Non-irrigated winter wheat/rapeseed/winter wheat/sunflower crop rotation since 2004 with recent introduction of a winter cover crop.

integrating relevant Earth Observation data. It calculates E through four sequential steps dedicated to the estimation of (i) E_{p}, (ii) interception loss (E_{i}), (iii) soil water content, and (iv) evaporative stress (S).

In GLEAM4, E_{i} is computed on rainy days using a global van Dijk–Bruijnzeel model (van Dijk and Bruijnzeel, 2001) constrained by satellite-observed vegetation data and a meta-analysis of past field experiments (Zhong et al., 2022). This implementation accounts for sub-grid heterogeneity by computing E_{i} over tall and short vegetation fractions separately, enabling a more realistic representation of this component (Zhong et al., 2022, 2024). E_{p} is calculated using Penman's equation (Miralles et al., 2025), unlike previous GLEAM versions that used the Priestley and Taylor formulation (GLEAM; Miralles et al., 2011); as such, it explicitly accounts for the influence of wind speed, vegetation height, and vapour pressure deficit (VPD) on E_{p}. Soil water dynamics are key in accurately estimating vegetative stress and consequently E; GLEAM4 uses a multi-layer running water balance accounting for plant access to groundwater, which plays an important role in certain vegetated areas during dry conditions (Hulsman et al., 2023). Microwave soil moisture, brightness temperatures, and/or backscatter observations are assimilated in the top soil layer (Martens et al., 2017; Miralles et al., 2025). Additionally, GLEAM4 accounts for understory and bare soil evaporation by modelling the transmission of incoming radiation through the canopy using the Beer-Lambert law based on leaf area index (LAI) (Miralles et al., 2025). In GLEAM4, the fractional cover of tall and short vegetation, bare soil, and open water is dynamic in space and time, as described by Zhong et al. (2022).

https://doi.org/10.5194/egusphere-2026-1856
Preprint. Discussion started: 10 April 2026

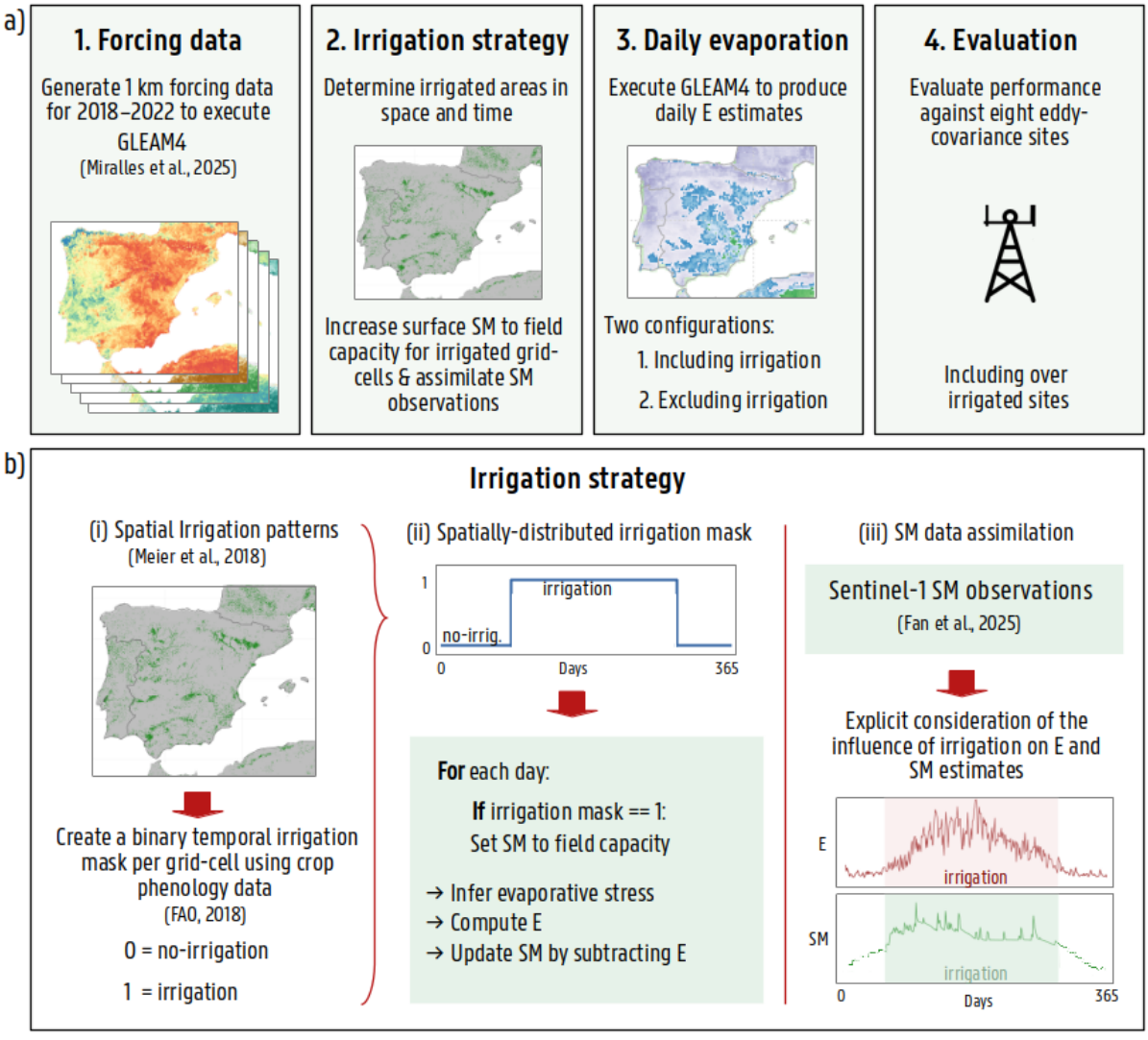

Figure 2. (a) Workflow of the proposed methodology to develop a daily high-resolution E dataset for 2018–2022 that includes the contribution of irrigation. (b) Proposed irrigation strategy, following three steps: (i) identification of times and locations where irrigation occurs by combining the irrigation map of Meier et al. (2018) with FAO's crop phenology data (FAO, 2018), (ii) increasing soil moisture (SM) prior to S computation, and (iii) Sentinel 1 SM data assimilation.

Arguably, one of the most critical components of GLEAM4 is the estimation of S over vegetated areas, which is based on a machine learning approach designed to capture how environmental stressors constrain E below E_p (Miralles et al., 2025). These stressors include vegetation properties and environmental variables such as soil plant-available water, VOD, air temperature, VPD, LAI, wind speed, shortwave incoming radiation (SW_i), and atmospheric CO_2 concentration (Koppa et al., 2022). In the current version, two extreme Gradient Boosting models (XGBoost; Chen and Guestrin, 2016) are trained to

https://doi.org/10.5194/egusphere-2026-1856
Preprint. Discussion started: 10 April 2026

predict S for tall and short vegetation fractional cover independently, using eddy-covariance and sap flow data across a wide variety of ecosystems (Koppa et al., 2022). S ranges from zero to one, where high S values indicate low vegetation stress, whereas low S values are associated with higher levels of vegetative stress and reduced transpiration relative to its potential.

3.2 Input data

To force GLEAM4 at high spatial resolution, we generated a 1 km forcing dataset using variable-specific downscaling procedures, partly based on the input datasets described in Miralles et al. (2025). This strategy ensures the global applicability of the methods presented here by relying on globally available datasets rather than region-specific products. An overview of the datasets used and the associated processing steps is provided in Table 2.

Precipitation and air temperature were downscaled from MSWEPv2.8 (Beck et al., 2019) and MSWXv1 (Beck et al., 2022), respectively, by computing and applying monthly correction factors leveraging the high-resolution monthly climatologies from CHELSAv2.1 (Karger et al., 2017) as done in recent studies (Filippucci et al., 2025). VPD was subsequently derived from the downscaled air temperature and humidity fields from MSWXv1 interpolated bilinearly to 1 km. Snow water equivalent (SWE) was obtained by merging daily estimates from GlobSnow (Luojus et al., 2021) and the AMSR-E/Aqua Daily L3 product by Tedesco et al. (2004), as the former does not provide SWE estimates over mountainous regions or the Global South.

Outgoing shortwave radiation (SW_u) and SW_i were derived by adapting the downscaling framework by Rains et al. (2024) based on Meteosat Second Generation (MSG) Land Surface Analysis Satellite Application Facility (LSA SAF; Trigo et al., 2011) and MODIS data. To compute SW_u, we used daily albedo and SW_i data. Albedo data from LSA SAF were downscaled using MODIS albedo (MCD43A2; Schaaf and Wang, 2021), while LSA SAF SW_i was resampled to 1 km through bilinear interpolation. Outgoing longwave radiation (LW_u) was computed using land surface temperature (LST), emissivity data, and incoming longwave radiation (LW_i). Emissivity was derived similarly to albedo, by downscaling LSA SAF emissivities using MODIS emissivity estimates (Wan et al., 2021), while LW_i was obtained by bilinearly interpolating LSA SAF estimates. To obtain consistent LST estimates, hourly clear-sky LST observations from LSA SAF (Ermida et al., 2018) were corrected and downscaled using the four daily MODIS LST overpasses (Terra and Aqua, day and night; Wan et al., 2021). First, MODIS LST observations were converted to UTC, screened using quality flags, and temporally normalised to the nearest LSA SAF acquisition time. Second, the MODIS overpasses were used to bias-correct the LSA SAF LST. A Kalman filter was then applied to assimilate the MODIS observations into the hourly MSG LST time series, resulting in a corrected continuous LST dataset. These continuous LST fields were subsequently aggregated to daily resolution and used to compute outgoing longwave radiation. The four radiation components (incoming and outgoing shortwave and longwave radiation) were then combined to estimate daily R_n at 1 km resolution. Remaining gaps inherited from the MSG observations were filled using a spatial interpolation approach based on neighbouring grid-cells. Further details can be found in Rains et al. (2024).

LAI and the fraction of absorbed photosynthetically active radiation (fAPAR) from MODIS (MCD15A2H v6.1; Myneni et al., 2021) were partitioned into tall and short vegetation fractions using MODIS vegetation continuous fields (MOD44B v6.1; DiMiceli et al., 2022). To minimise vegetation-type mixing, LAI and fAPAR were averaged within a 7 km moving window over areas where tall or short vegetation fractions exceeded the 95th percentile according to MOD44B, following the

https://doi.org/10.5194/egusphere-2026-1856
Preprint. Discussion started: 10 April 2026

approach of Zhong et al. (2022) but at higher spatial resolutions. Soil hydraulic properties from HiHydrosoil v2 (Simons et al., 2020) and vegetation height from the GLAD Global Land Cover and Land Use Change dataset (Potapov et al., 2022) were aggregated from their native resolutions of 250 m and 30 m, respectively.

In addition, as part of the irrigation strategy adopted in this study, the global irrigation map (30 arcsec) of Meier et al. (2018) was used. It is derived from a wide range of data sources, including land cover, temporal Normalised Difference Vegetation Index (NDVI) dynamics, agricultural suitability, cropping potential, and the Global Map of Irrigation Areas (GMIA) from Siebert et al. (2005) representative of conditions in 2018. This product was validated against several widely used global and regional irrigation datasets. Unlike the FAO definition of irrigated areas, which identifies areas equipped for irrigation, the dataset of Meier et al. (2018) identifies areas that are actually irrigated. This distinction is critical for E modelling, as irrigation-equipped areas are not necessarily irrigated every year or season (McDermid et al., 2023). By focusing on effective irrigation rather than potential irrigation extent, this dataset provides a more appropriate basis for representing irrigation impacts on E within a physically consistent modelling framework. To represent the temporal evolution of irrigation, the crop phenology dataset (30 arcsec) from FAO's Agricultural Stress Index System (ASIS; FAO, 2018) was used. It characterises the phenological cycle by distinguishing three main stages: the start of the season (early crop development), the peak (full crop development), and the end of the season (physiological maturity). The dataset covers up to two crop seasons per year and is derived from NDVI dynamics at the grid-cell level. The end-of-season phase corresponds to physiological maturity and does not necessarily coincide with harvest. Finally, 1 km surface soil moisture estimates from the S1-DPA dataset, based on Sentinel-1 dual-polarisation SAR measurements (Fan et al., 2025), were assimilated.

3.3 Irrigation representation

To represent irrigation effects on E in a framework suitable for future integration into the GLEAM4 global products, we adopt a scalable four-step strategy: (i) identifying the locations and periods when irrigation occurs, (ii) increasing soil moisture to field capacity in the corresponding grid-cells and periods prior to the computation of S, (iii) predicting S to constrain E below E_{p} and subtracting the water lost through E from the soil, and (iv) assimilating soil moisture observations to dynamically constrain irrigation inputs and ensure realistic soil moisture variability. This approach allows irrigation dynamics to be represented at a daily temporal scale while relying on datasets that can be consistently applied across the global domain.

The timing and spatial distribution of irrigation are determined by combining the global irrigation map from Meier et al. (2018) with crop phenology information from the FAO Agricultural Stress Index System (FAO, 2018). Specifically, the static irrigation map is used to delineate irrigated areas, while the phenology dataset is used to identify the periods of active irrigation, assumed to extend from the start to the end of the growing season. This combination results in a daily irrigation mask indicating the irrigation calendar, not the actual days on which irrigation is applied. grid-cells are flagged as irrigated (value of one) during active crop growth and non-irrigated (value of zero) otherwise. The resulting dataset is rescaled to the 1 km GLEAM grid using a nearest-neighbour interpolation scheme and applied consistently across the study period (2018–2022).

For grid-cells and periods identified as irrigated, soil moisture is increased to field capacity within the short vegetation fraction of each grid-cell before the computation of S. Because the short vegetation fraction is dynamically modulated by

Table 2. Overview of input datasets and processing steps used to produce the 1 km forcing data to execute GLEAM4 at high resolution in this study.

Variable	Source(s)	Processing scheme	References
Net radiation (R_n)	LSA SAF / MODIS	Derived by adapting the approach of Rains et al. (2024). LSA SAF emissivity and albedo were downscaled using MODIS (MOD11A1 and MCD43A2) data. Hourly LSA SAF LST was bias-corrected with MODIS 1 km LST using a Kalman filter.	(Trigo et al., 2008; Ermida et al., 2018; Wan et al., 2021; Schaaf and Wang, 2021)
Shortwave incoming (SW_i)	LSA SAF	Downscaled to 1 km through bilinear interpolation, following Rains et al. (2024).	Trigo et al. (2008); Carrer et al. (2019)
Shortwave outgoing (SW_u)	LSA SAF / MCD43A2	Derived from downscaled LSA SAF SW_i and downscaled LSA SAF-based surface albedo by adapting the approach of Rains et al. (2024).	(Trigo et al., 2008; Carrer et al., 2019; Schaaf and Wang, 2021)
Air temperature (T_a)	MSWXv1 / CHELSAv2.1	MSWXv1 data downscaled to 1 km using CHELSAv2.1 monthly climatologies through monthly additive correction factors.	Beck et al. (2022); Karger et al. (2017)
Precipitation (P)	MSWEPv2.8 / CHELSAv2.1	MSWEPv2.8 downscaled to 1 km using CHELSAv2.1 monthly climatologies, including precipitation undercatch corrections for high elevations and snow-covered areas through monthly multiplicative correction factors.	Beck et al. (2019); Karger et al. (2017)
Vapour pressure deficit (VPD)	MSWXv1	Computed from downscaled T_a and humidity data (interpolated bilinearly to 1 km).	Beck et al. (2022)
CO_2 concentration	CAMS	Interpolated bilinearly to 1 km.	Inness et al. (2019)
Wind speed (u)	ERA5	Calculated from the eastward and northward wind components using the Pythagorean theorem and subsequently interpolated bilinearly to 1 km.	Hersbach et al. (2020)
Snow water equivalent (SWE)	GlobSnow / AMSR-E/Aqua	GlobSnow and AMSR-E merged at 0.1° to better represent complex topography and interpolated bilinearly to 1 km.	Luojus et al. (2021); Tedesco et al. (2004)
Vegetation optical depth (VOD)	VODCA v2	Interpolated bilinearly to 1 km.	Zotta et al. (2024)
Leaf area index (LAI)	MOD15A3H/ MOD44B	Partitioned into tall and short fractions using MOD44Bv6.1 vegetation data. Fractional LAI estimated per grid-cell by averaging LAI values in a 7 km window where tall/short vegetation exceeded the 95th percentile of vegetation cover fraction, adapted from Zhong et al. (2022).	Myneni et al. (2021); DiMiceli et al. (2022)
Fraction of absorbed PAR (fAPAR)	MOD15A3H/ MOD44B	Processed as for LAI, adapted from Zhong et al. (2022).	Myneni et al. (2021); DiMiceli et al. (2022)
Vegetation height	GEDI / Landsat	Averaged to 1 km from native 30 m resolution.	Potapov et al. (2022)
Soil properties	HiHydroSoil	Averaged to 1 km from native 250 m resolution.	Simons et al. (2020)
Surface soil moisture (SM_s)	S1-DPA	Retrieved from Sentinel-1 dual-polarisation SAR observations using a forward-model inversion algorithm. The S1-DPA product provides global 1 km estimates with a 3–6 day revisit over Europe and high accuracy over croplands.	Fan et al. (2025)
Irrigation	Global irrigation map / FAO ASIS	Dynamic daily maps combining the global irrigation map from Meier et al. (2018) with crop phenology information from the FAO Agricultural Stress Index System.	Meier et al. (2018); FAO (2020)

https://doi.org/10.5194/egusphere-2026-1856
Preprint. Discussion started: 10 April 2026

https://doi.org/10.5194/egusphere-2026-1856
Preprint. Discussion started: 10 April 2026

fAPAR (Zhong et al., 2022), the effective irrigation signal also follows the seasonal dynamics of vegetation. This design reduces potential biases associated with false positives in the irrigation mask, while representing irrigation under a near-ideal case. The approach alleviates water stress for irrigated vegetation relative to non-irrigated areas, while allowing other environmental stressors known to regulate stomatal conductance — such as VPD (atmospheric dryness), air temperature (heat stress), SW_i (PAR availability), and atmospheric CO_2 concentration (stomatal regulation) — to constrain E below its potential rate (Koppa et al., 2022). When soil moisture is already at field capacity due to precipitation, no additional irrigation is applied.

To further increase the realism of irrigation amounts and ensure consistency with observed soil moisture dynamics, high-resolution surface soil moisture observations are assimilated. We use the global 1 km S1-DPA dataset (Fan et al., 2025), which provides Sentinel-1–based soil moisture estimates derived using a dual-polarisation retrieval algorithm that minimises mismatches between simulated and observed backscatter while accounting for variations in soil and vegetation conditions. The dataset offers near-global coverage, with a revisit time of 3–6 days over Europe, and has demonstrated particularly strong performance over croplands, making it well suited for hydrological and agricultural applications (Fan et al., 2025).

Soil moisture assimilation follows the sequential approach of Martens et al. (2017) and Miralles et al. (2025), in which observed soil moisture anomalies are first computed and scaled to match the climatology of the GLEAM4 open-loop soil moisture estimates (here including irrigation) using a Newtonian nudging scheme. The assimilation is applied to the top soil layer (0–5 cm) throughout the study area, including both irrigated and non-irrigated grid-cells. The updated values are subsequently propagated to deeper layers by the process-based model. By constraining the temporal evolution of soil moisture with data assimilation, this approach ensures that soil moisture dynamics, and consequently irrigation amounts, remain consistent with satellite-observed variability at high spatial resolution.

3.4 Performance evaluation

To assess the performance of the high-resolution GLEAM4 E estimates, we evaluated them against the selected *in situ* E measurements presented in Table 1 and Figure 1. As a metric of performance, we used the modified Kling–Gupta efficiency (KGE; Gupta et al., 2009; Kling et al., 2012), which summarises model performance in terms of Pearson's correlation coefficient (r), the bias ratio (β), and the variability ratio (γ). The KGE is computed as:

$$\mathrm{KGE} = 1 - \sqrt{(r-1)^2 + (\beta-1)^2 + (\gamma-1)^2}, \tag{1}$$

where:

$$r = \frac{\sum_{i=1}^{n}(O_i - \overline{O})(S_i - \overline{S})}{\sqrt{\sum_{i=1}^{n}(O_i - \overline{O})^2}\sqrt{\sum_{i=1}^{n}(S_i - \overline{S})^2}}, \quad \beta = \frac{\overline{S}}{\overline{O}}, \quad \text{and} \quad \gamma = \frac{\sigma_S/\overline{S}}{\sigma_O/\overline{O}}, \tag{2}$$

with O_i and S_i denoting the observed and simulated values, respectively, $\overline{O}$ and $\overline{S}$ their means, and σ_O and σ_S their standard deviations. KGE values range from $-\infty$ to 1, with values closer to 1 indicating better agreement between simulated and observed E.

https://doi.org/10.5194/egusphere-2026-1856
Preprint. Discussion started: 10 April 2026

4 Results and discussion

4.1 Contribution of irrigation in E estimates

Figure 3 shows the spatial distribution of mean annual E based on 1 km GLEAM4 with and without irrigation over the study period (2018–2022). Clear increases in E associated with irrigation appear along the riparian zones of the Ebro River and its tributaries, as well as in the Duero, Guadiana, and Guadalquivir river basins, all of which are intensively irrigated (Tocados-Franco et al., 2023; Playán et al., 2024). Increases in annual E due to irrigation reach up to approximately 450 mm, effectively doubling E compared to simulations without irrigation (Fig. 3c), consistent with the 100–500 mm irrigation volumes across the Ebro Basin reported by Dari et al. (2023). Similar increases in E have also been reported by Dari et al. (2024b) when irrigation water use is explicitly represented in land surface model simulations. Furthermore, the spatial patterns of irrigation-induced increases in E align well with those in the European Crop-specific Irrigated Area (ECIRA) dataset over the Iberian Peninsula (Zhu et al., 2025), indicating that the applied irrigation mask accurately captures the spatial distribution of irrigated areas relative to an independent dataset. However, this comparison is not fully independent, since both ECIRA and the global irrigation map of Meier et al. (2018) incorporate the GMIA dataset from Siebert et al. (2005).

The influence of irrigation also varies substantially inter-annually depending on regional water availability. For example, the mean annual increase in E attributed to irrigation was 76 mm yr^{-1} in 2018, whereas in 2022 it reached 246 mm yr^{-1}. This difference reflects the contrasting hydroclimatic conditions during the study period: 2018 was relatively wet, while in 2022 an exceptional drought affected the Iberian Peninsula (Serrano-Notivoli et al., 2023; Garrido-Perez et al., 2024). These results suggest that the implemented strategy captures the increased irrigation demand associated with reduced water availability; it will not capture, however, potential top-down irrigation restrictions imposed by water authorities or reductions in irrigation due to insufficient water availability during periods of drought.

Spatial patterns of irrigated areas also broadly agree with those reported by Dari et al. (2023), although their mapped extent is noticeably larger. This difference likely stems from their soil moisture inversion method, which estimates irrigation by attributing all water inputs inferred from soil moisture changes over croplands to precipitation plus irrigation. Because their method depends on daily consistency between the selected soil moisture and precipitation datasets, noise or mismatches between the soil moisture and precipitation signals can artificially inflate irrigation estimates and lead to the misclassification of non-irrigated areas as irrigated. This is consistent with the limitations noted by Dari et al. (2023); Zappa et al. (2024), including spurious irrigation signals in non-irrigated regions and false irrigation activity during non-irrigated periods. Similar challenges were reported by Purnamasari et al. (2025), particularly in humid regions when detecting irrigated areas using land surface temperature combined with a hydrological model. Consequently, the magnitudes over the Ebro Basin in Figure 3c are not directly comparable to those reported by Dari et al. (2023), and lower values are expected here as Dari et al. (2023) estimate actual irrigation amounts by scaling E with an irrigation efficiency factor (typically 15–30%; Dari et al., 2020), whereas here we quantify only the increase in E attributable to irrigation.

https://doi.org/10.5194/egusphere-2026-1856
Preprint. Discussion started: 10 April 2026

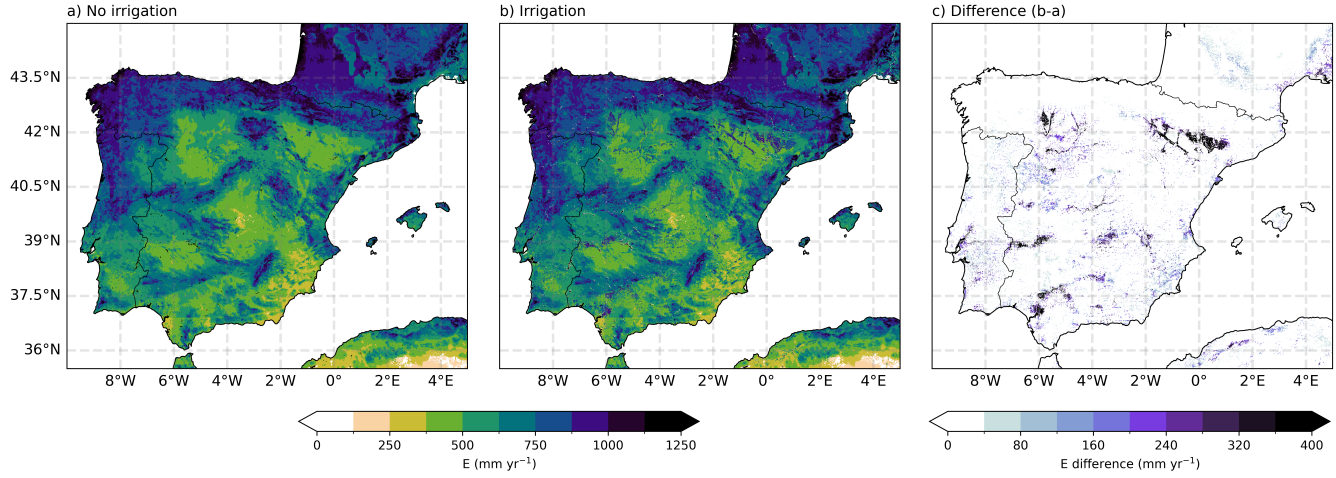

Figure 3. Mean annual E estimates for 2018–2022 for: (a) the model run without irrigation and soil moisture data assimilation, (b) the model run including the irrigation strategy, and (c) the difference between both runs $(b - a)$, representing the additional E attributable to irrigation.

4.2 Ability to capture *E* dynamics

We evaluated the performance of the E estimates at the daily temporal scale using a total of eight eddy-covariance sites: six over non-irrigated areas, and two over irrigated areas. Daily KGE values span 0.17–0.64, highlighting the large spread in performance and differences in the ability to capture high-frequency daily E variability.

The spatial distribution of all selected stations is shown in Figure 4. Figure 4a shows the performance of all evaluated eddy-covariance sites using the KGE and its components. Non-irrigated sites are shown in purple, while irrigated sites are shown in green. For the irrigated sites, both experiments are presented: (i) including the irrigation strategy (dark green) and (ii) the benchmark without irrigation (light green). For the sites without irrigation (panel a), the highest performance is observed in central Spain (ES-LM1, ES-LM2, and ES-Abr), where daily KGE values range from 0.53 to 0.64. In contrast, lower scores are obtained in non-irrigated sites from southeastern Spain (ES-LJu and ES-Agu), with daily KGE values between 0.17 and 0.32. The reduced skill at these sites is most evident in the correlation component (r), which reflects the temporal dynamics of E, and is particularly low at ES-LJu. This behaviour is expected, as this region exhibits the highest aridity index across the Iberian Peninsula and thus precipitation can lead to highly episodic soil moisture and E dynamics (Beguería et al., 2025). Moreover, estimating E in arid and semi-arid regions is inherently challenging due to the strong sensitivity to short-lived wetting events and the rapid drying of the surface layer, leading to consistently lower performance in terms of E (Nelson et al., 2024; Miralles et al., 2025). Under such conditions, even small uncertainties in precipitation, soil moisture, or vegetation descriptors can translate into large relative errors in daily E, and timing mismatches become more critical because E responds almost instantaneously to precipitation (and irrigation). Additionally, the Sentinel-1–based 1 km S1-DPA soil moisture product (C-band SAR) is disproportionally affected by subsurface scattering over dry soils, potentially generating anomalous backscatter signals and

https://doi.org/10.5194/egusphere-2026-1856
Preprint. Discussion started: 10 April 2026

degrading soil moisture retrieval accuracy (Wagner et al., 2022). Despite these challenges, the performance over Mediterranean sites remains encouraging: daily KGE values fall within the expected range with a median KGE for non-irrigated sites of 0.53, which is consistent with the global performance of coarse-resolution GLEAM4 (Miralles et al., 2025).

Regarding irrigated sites, La Cendrosa (Boone et al., 2025), located in the Ebro Basin, shows a marked improvement when irrigation is included, with daily KGE increasing from –0.48 to 0.19. This improvement is driven by gains across all components, particularly r (–0.20 to 0.39) and β (0.41 to 0.78), while γ moves closer to one, decreasing from 1.63 to 0.52, indicating remaining limitations in capturing temporal variability. Similarly, ES-Cnd in southern Spain shows improved performance, with KGE increasing from 0.21 to 0.40, accompanied by performance increases in r (0.36 to 0.45), β (0.61 to 0.76), and γ (1.26 to 0.93).

Figure 4*b* presents the subset of sites classified as irrigated by the dynamic mask, including three non-irrigated sites (purple) that were incorrectly flagged (ES-LM1 and ES-LM2 are located in very close proximity). Results are shown for both experiments: with irrigation (darker colours) and without (lighter colours). These results highlight the impact of false-positive irrigation detection on E estimates. At ES-LM1 and ES-LM2, performance decreases slightly due to changes in bias and variability (KGE from 0.59 to 0.54 and 0.63 to 0.53, respectively), while FR-Aur shows a small improvement (0.38 to 0.41). Overall, these effects are minor compared to the improvements observed at genuinely irrigated sites, indicating that the model is relatively robust to false-positive irrigation signals. This robustness arises from (i) the aggregation of independent vegetation fractions in GLEAM, with seasonality driven by fAPAR (Zhong et al., 2022), which limits the contribution of short vegetation during dry periods, and (ii) the seasonal alignment between precipitation and the growing season of non-irrigated sites, which reduces the relative impact of additional irrigation inputs. Consequently, misclassified irrigation signals have a limited effect on soil moisture dynamics and E estimates.

Figure 5 shows (a) the 2021 time series for the La Cendrosa site over the irrigated season (May–October) and (b) the 2018–2020 period for the irrigated ES-Cnd site. Both figures include E (top), S (middle), and surface soil moisture estimates (bottom). It is evident that the experiment including irrigation reproduces the observed E dynamics more accurately than the no-irrigation case for both stations. In the latter, E decreases rapidly as the soil dries, driven by increasing vegetation stress (low S values that suppress E_{p}). This behaviour reflects the high sensitivity of S in arid regions to short-lived wetting events, which lead to rapid soil moisture depletion and reduced plant-available water, further constraining E. In contrast, when irrigation is included and soil moisture increases, vegetative stress decreases, resulting in S values closer to 1, as expected from enhanced plant-available water. Accurately representing S is important, as prolonged vegetative stress can impact vegetation and even alter plant physiology (Kan et al., 2023), including under well-watered conditions (Julia and Dingkuhn, 2013). Despite this, an increase in vegetative stress (lower S values) is observed between May and July at both sites. These patterns highlight the importance of accounting for multiple stress factors, as plant functioning is influenced not only by water and energy availability but also by variables such as wind speed, leaf morphology and physiology, heat stress, and VPD (Koppa et al., 2022; Jagadish et al., 2021; Lambers and Oliveira, 2019).

https://doi.org/10.5194/egusphere-2026-1856
Preprint. Discussion started: 10 April 2026

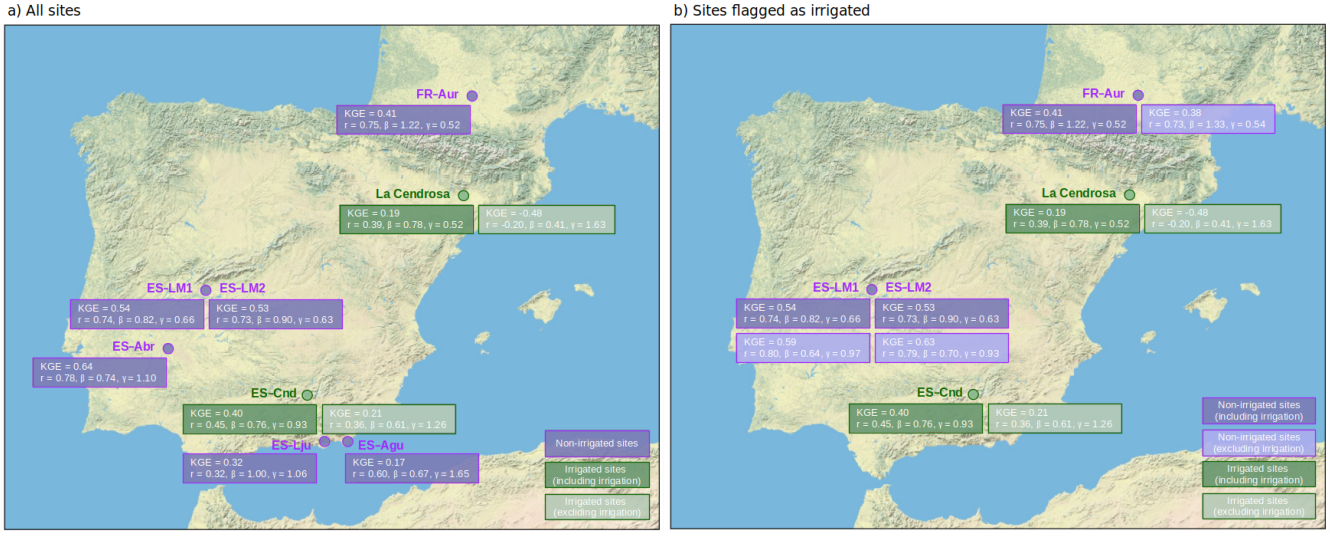

Figure 4. Performance of GLEAM4 E estimates at eddy-covariance sites using the KGE and its components. (a) All evaluated sites, distinguishing non-irrigated (purple) and irrigated (green) locations. For irrigated sites, results are shown for both experiments: with irrigation (dark green) and without irrigation (light green). (b) Subset of sites classified as irrigated by the dynamic mask, including three non-irrigated sites incorrectly identified as irrigated (purple). Results are shown for simulations with irrigation (darker colours) and without irrigation (lighter colours).

4.3 Evaporation partitioning over the Iberian Peninsula

Figure 6 shows the spatial distribution of the components (E_t, E_i, and E_b) of mean annual total E for 2018–2022, based on the experiment that includes irrigation (see Figure 3b). The highest E values are located in the northern Iberian Peninsula (Galicia, Asturias, Cantabria, Basque Country, and northern Aragón) and along the Mediterranean coast of Catalonia and Valencia, often exceeding 800 mm yr^{-1}. These regions are dominated by closed forests (see Figure 1b). High E values are also observed across northern Portugal and in forested and mountainous regions, particularly in the Central System (Castilla), Iberian System (Aragón), and Sierra Morena (Andalusia), with totals between 500 and 700 mm yr^{-1} (Figure 3b). The spatial patterns and magnitudes of E presented in this study are consistent with those in other state-of-the-art E datasets (Nelson et al., 2024; Miralles et al., 2025).

Overall, E_t is the dominant contributor to total E, with values typically ranging from near zero in dry steppe areas to more than 700 mm yr^{-1} in dense forests, where it accounts for approximately 60–80% of total E. In more sparsely vegetated regions, its relative contribution decreases to about 30–60%, although increases are observed over irrigated areas such as those in the Ebro Basin. E_i is higher in densely vegetated regions (see also Figure 1b). In relative terms, E_i generally contributes up to 20% of total E mainly over forested regions in Galicia, Cantabrian Coast, and Pyrenees. E_b typically ranges between 0 and 400 mm yr^{-1}, with the highest values in sparsely vegetated regions. Its relative contribution varies from about 10–30% in densely vegetated regions to as much as 80% across the Spanish dry steppes.

https://doi.org/10.5194/egusphere-2026-1856
Preprint. Discussion started: 10 April 2026

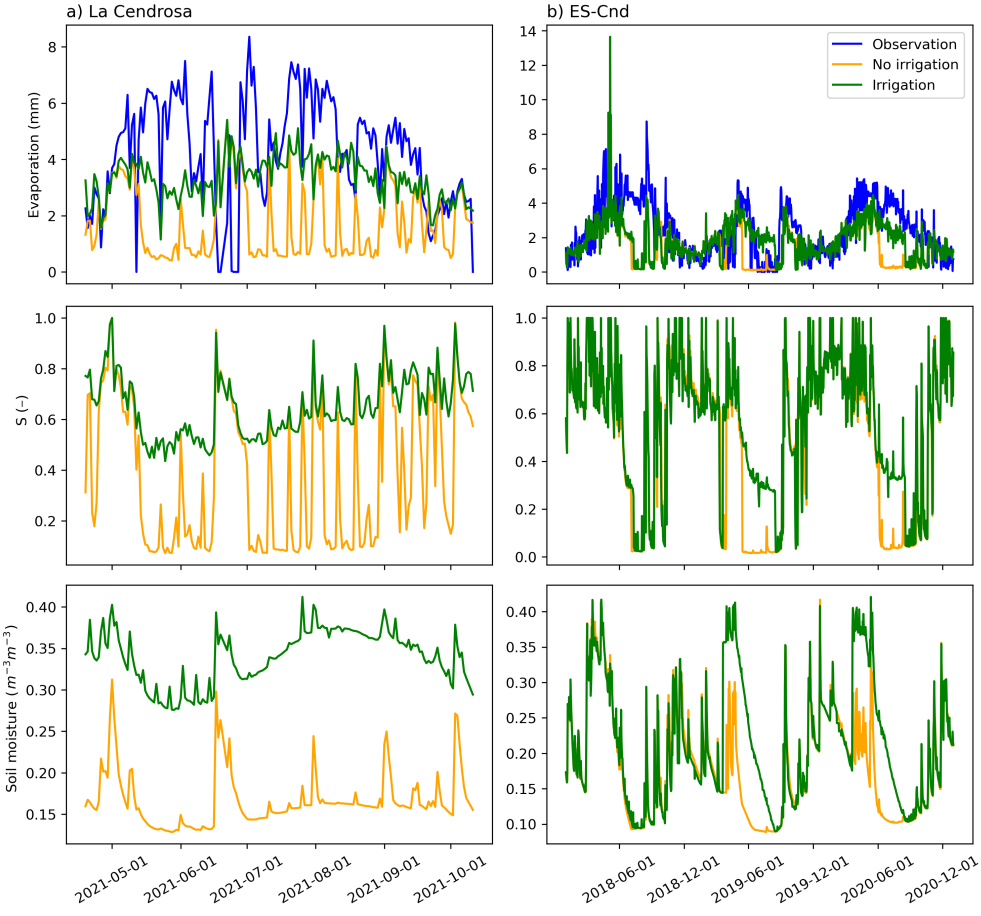

Figure 5. Time series of E (top), S (middle), and soil moisture (bottom) at the La Cendrosa site (left panel), located within the Ebro Basin, and ES-Cnd (right panel). The blue line represents observed E, while the green and yellow lines depict estimates for the irrigated and non-irrigated experiments, respectively.

Figure 7 illustrates winter (DJF; December–February) and summer (JJA; June–August) conditions for E and its components over the period 2018–2022. E exhibits pronounced seasonal variability across the Iberian Peninsula, with higher values over northern Spain (Galicia, the Cantabrian Cordillera, the Basque Country, and the Pyrenees), largely driven by the seasonality of E_t. Maximum values occur during summer in forested regions due to increased energy and water availability, whereas minimum values are observed during summer in water-limited regions, particularly in Andalusia and Castilla. E_i displays lower seasonal variability, as it primarily responds to precipitation patterns, particularly in the more densely vegetated regions of the northern Iberian Peninsula where precipitation is more frequent. In contrast, E_b reaches higher values during winter in the sparsely vegetated regions of central-western Spain, while remaining relatively low in summer due to strong water limitations during the dry season.

https://doi.org/10.5194/egusphere-2026-1856
Preprint. Discussion started: 10 April 2026

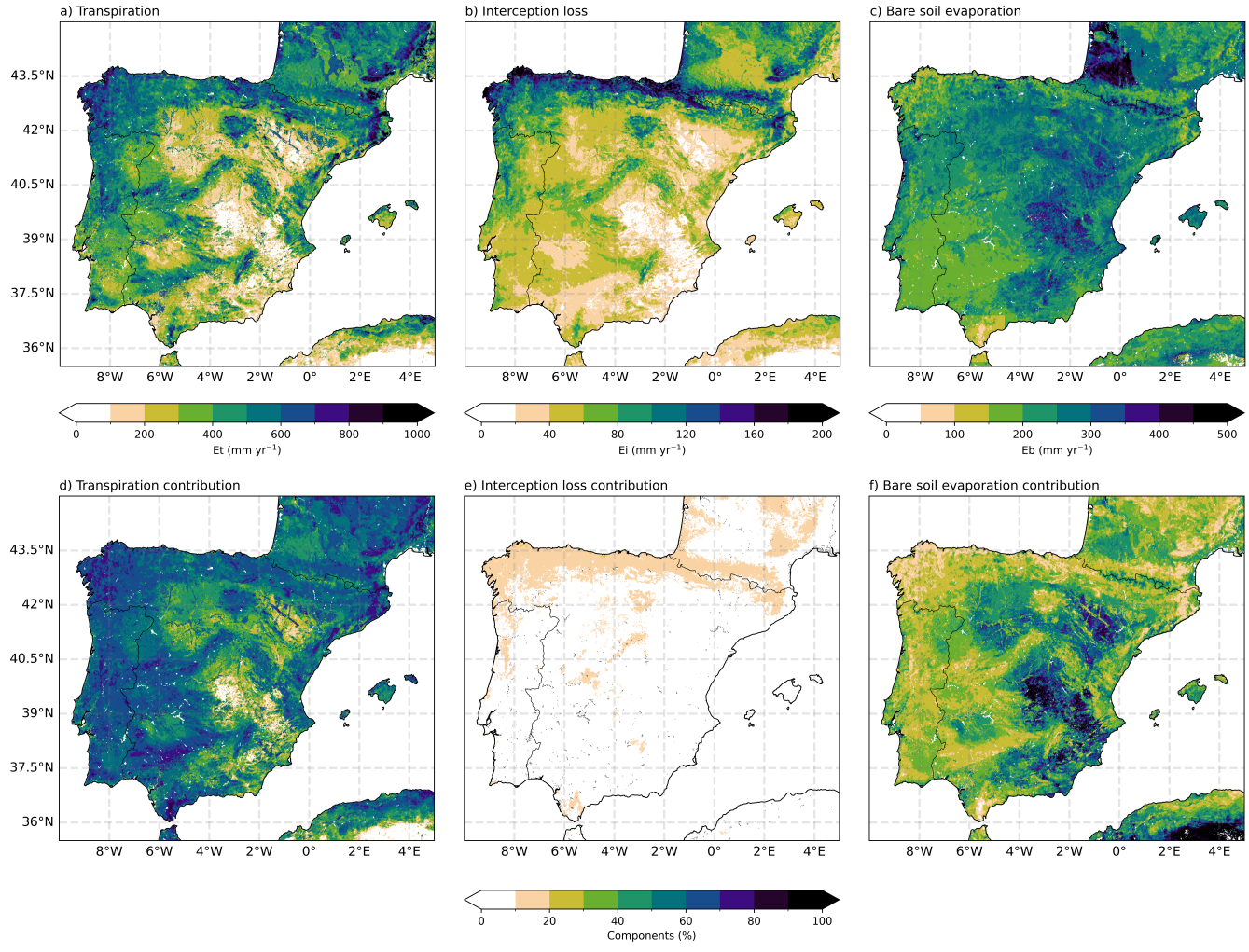

Figure 6. Mean annual E components (2018–2022) over the Iberian Peninsula considering irrigation: (a) transpiration (E_t), (b) interception loss (E_i), and (c) bare soil evaporation (E_b). Their contribution to total E in percentage is shown in panels d–f for E_t, E_i, and, E_b, respectively.

4.4 Limitations and future work

Among the main limitations of the approach presented here is that irrigated areas have expanded or shifted rapidly due to changes in agricultural practices, water availability, and policy incentives (McDermid et al., 2023). Using a temporally fixed irrigation map therefore introduces uncertainties in both the spatial extent and timing of irrigation, which ultimately depend on crop type and human management decisions. In addition, irrigation is represented here under a near-ideal assumption, whereby soil moisture is increased to field capacity rather than explicitly modelling actual irrigation applications. This may affect

https://doi.org/10.5194/egusphere-2026-1856
Preprint. Discussion started: 10 April 2026

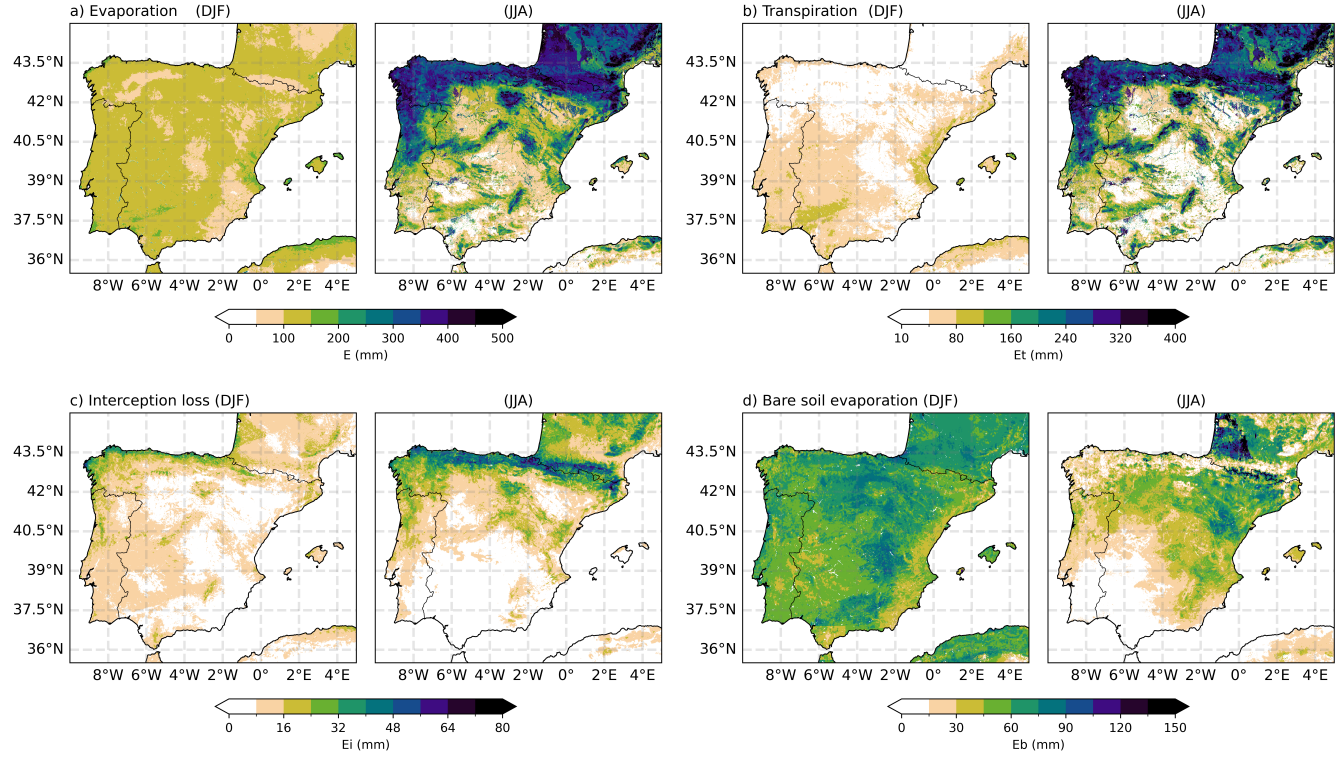

Figure 7. Seasonal E (panel a) and its components E_{t}, E_{i}, and E_{b} (panels b–d, respectively) during winter (DJF; December–February) and summer (JJA; June–August) for 2018–2022.

irrigation estimates in cases where farmers adopt deficit irrigation strategies, commonly applied to crops such as olive trees and grapevines (Expósito and Berbel, 2017; Domingo and Castel, 2010). Moreover, the Sentinel-1–based 1 km S1-DPA soil moisture product used in this study may also be affected by subsurface scattering over dry soils, which can generate anomalous backscatter signals and reduce soil moisture retrieval accuracy (Wagner et al., 2022).

Future work should therefore focus on developing methods that combine multiple complementary data sources (e.g., land surface temperature, vegetation dynamics, microwave backscatter, gravimetric observations, census information, and local irrigation statistics) to produce long-term global dynamic irrigation datasets. Because the FAO crop phenology dataset is derived from NDVI, it could, in principle, support the development of dynamic interannual irrigation maps by applying thresholds to vegetation indices. For example, Maselli et al. (2020) combined meteorological data with Sentinel-2 NDVI observations to estimate E over irrigated Mediterranean croplands by identifying vegetated areas and their temporal evolution, thereby assessing where water inputs exceeded precipitation alone. Similar approaches are commonly used in land surface irrigation modelling, where irrigation timing is inferred from satellite-based or modelled vegetation indicators (Modanesi et al., 2022). The need for improved irrigation information aligns with the priorities expressed by agricultural stakeholders in the community consultation of Massari et al. (2021), who emphasised the importance of irrigation datasets at spatial resolutions of 1 km or finer.

https://doi.org/10.5194/egusphere-2026-1856
Preprint. Discussion started: 10 April 2026

Nevertheless, irrigation remains one of the most uncertain components of the global water cycle, with its contribution to total water withdrawals ranging from approximately 45% to 90%, depending on the region and methodology (Puy et al., 2025). Key challenges in developing consistent and accurate estimates of irrigation extent and volume include (i) the limited availability of *in situ* data, (ii) coarse reporting at the irrigation-district scale rather than at the plot level (Massari et al., 2021), which limits the distinction between actively irrigated areas and those merely equipped for irrigation (Dari et al., 2023), and (iii) biases in census-based datasets due to farmers' self-reporting, influenced by economic incentives, policy requirements, and limited monitoring capacity (McDermid et al., 2023).

5 Conclusions

This study developed a framework for estimating daily E at high spatial resolution (1 km) based on GLEAM4, applied to the Iberian Peninsula. Because irrigation strongly influences E at these spatial scales, a novel irrigation strategy was proposed consisting of: (i) identifying locations and periods where irrigation occurs, (ii) increasing soil moisture prior to the computation of S, and (iii) assimilating 1 km Sentinel-1-based soil moisture to constrain soil moisture dynamics. Two model configurations, one including irrigation and one excluding it, were used to quantify the contribution of irrigation to E and to evaluate the added value against *in situ* measurements. High-resolution (1 km), daily E estimates that account for irrigation practices are particularly valuable for proactive regional management strategies, where users often require information at high temporal resolution (Massari et al., 2021). As the workflow presented in this manuscript is designed to be globally applicable, it brings GLEAM4 closer to user needs in the water management and agricultural sectors.

A central innovation of this study is that the representation of irrigation does not rely on the assumption that irrigated crops evaporate at or near E_{p}. This assumption, used in several large-scale irrigation-detection algorithms, implicitly neglects non-hydrological stress factors such as VPD, heat stress, vegetation structure, wind speed, and CO_2 concentration. In contrast, our approach enables E to remain physically constrained by a diverse set of environmental drivers. As a result, irrigated crops are not forced to evaporate at E_{p} when environmental stressors would otherwise limit transpiration,thereby improving realism under conditions where multiple environmental stressors regulate plant functioning.

The validation demonstrates that the incorporation of irrigation improves the representation of E dynamics over irrigated sites. Daily KGE values increase at the two irrigated eddy-covariance stations, with improvements in correlation, bias, and variability. Increases in E related to irrigation reach up to 450 mm yr^{-1}, often doubling E compared to simulations that did not account for irrigation. These estimates are consistent with previous estimates for the Ebro Basin, and spatial patterns largely align with independent irrigation datasets. False positives in the irrigation mask have only limited impact on model performance, reflecting the robustness of GLEAM4, which is constrained by fractional-vegetation approach used to compute E.

The resulting 1 km dataset also captures the expected hydroclimatic gradients and spatial patterns of E across the Iberian Peninsula. Mean annual E is highest in the humid, forested regions of northern Spain and lowest in the semi-arid southeast, with E_{t} dominating total E in densely vegetated areas and E_{b} contributing more strongly in sparsely vegetated landscapes.

https://doi.org/10.5194/egusphere-2026-1856
Preprint. Discussion started: 10 April 2026

Evaluation against eight eddy-covariance sites indicates that the dataset provides a realistic representation of E variability at the daily scale across contrasting hydroclimates, with clear improvements at irrigated sites when irrigation is considered. E_{t} accounts for approximately 60–80% of total E in densely vegetated regions, decreasing to 30–60% in sparser areas, while E_{i} contributes up to 20% mainly in forested regions and E_{b} ranges from about 10–30% in vegetated areas to as much as 80% across the Spanish deserts. The dataset also captures pronounced seasonality, with peak E during summer over northern regions and reduced values in water-limited southern areas. In contrast, E_{i} follows precipitation patterns with lower seasonal variability, while E_{b} is higher during winter in sparsely vegetated regions and lower during the dry summer.

Overall, this work demonstrates that aiming to represent the influence of irrigation into a hybrid physically constrained E model can substantially enhance its estimates in agricultural landscapes. The approach provides a foundation for future global applications and supports improved monitoring of water use in regions where climate change, increasing aridity, and agricultural intensification are exacerbating the already growing pressure on freshwater resources. In addition, the dataset offers added value for land surface and climate modelling communities, as comparisons with E datasets that consider irrigation can help assess how models represent irrigation and its influence on coupled water and carbon cycles.

Data availability. The high-resolution E dataset and its components are publicly available through www.gleam.eu.

Author contributions. OMBV and DGM conceptualised the research. OMBV and DGM designed the computational framework. OMBV and AC performed the model runs and analysed the data. AC implemented the validation framework. All authors contributed to the interpretation of the results and writing of the manuscript.

Competing interests. At least one of the (co-)authors is a member of the editorial board of Hydrology and Earth System Sciences.

Acknowledgements. We thank Pere Quintana-Seguí, Anaïs Barella-Ortiz, and Roger Clavera-Gispert for providing data from the La Cendrosa site. The authors also acknowledge support from the Belgian Federal Science Policy Office (BELSPO) through the Stereo IV Earth Observation research programme, specifically the project *Hybrid Estimation and Remote Sensing Monitoring of Evaporation and Soil Moisture* (HERMES; contract no. SR/02/402). In addition, we acknowledge the European Space Agency for supporting the following projects: GLEAM-HR (contract no. RFP/3-18932/25/I-KE-bgh), DTE-Hydrology Next (contract no. AO/1-12108/24/I-KE), and *AGricultural Land AbandoNment and ClimatE change* (GLANCE; contract no. ESA/AO/1-12062/23/I-NB).

https://doi.org/10.5194/egusphere-2026-1856
Preprint. Discussion started: 10 April 2026

References

Allen, R. G., Tasumi, M., and Trezza, R.: Satellite-based energy balance for mapping evapotranspiration with internalized calibration (METRIC)—Model, Journal of irrigation and drainage engineering, 133, 380–394, https://doi.org/https://doi.org/10.1061/(ASCE)0733-9437(2007)133:4(380), 2007.

Alvarez, I., Pereira, H., Lorenzo, M., Picado, A., and Dias, J.: Assessing the performance of the CERRA dataset in reproducing precipitation and extreme precipitation events over the Iberian Peninsula, Journal of Hydrology: Regional Studies, 60, 102 517, https://doi.org/https://doi.org/10.1016/j.ejrh.2025.102517, 2025.

Anderson, M. C., Norman, J., Diak, G., Kustas, W., and Mecikalski, J.: A two-source time-integrated model for estimating surface fluxes using thermal infrared remote sensing, Remote sensing of environment, 60, 195–216, https://doi.org/https://doi.org/10.1016/S0034-4257(96)00215-5, 1997.

Bastiaanssen, W. G., Menenti, M., Feddes, R., and Holtslag, A.: A remote sensing surface energy balance algorithm for land (SEBAL). 1. Formulation, Journal of hydrology, 212, 198–212, https://doi.org/https://doi.org/10.1016/S0022-1694(98)00253-4, 1998.

Beck, H. E., Wood, E. F., Pan, M., Fisher, C. K., Miralles, D. G., Van Dijk, A. I., McVicar, T. R., and Adler, R. F.: MSWEP V2 global 3-hourly 0.1 precipitation: methodology and quantitative assessment, Bulletin of the American Meteorological Society, 100, 473–500, https://doi.org/https://doi.org/10.1175/BAMS-D-17-0138.1, 2019.

Beck, H. E., Van Dijk, A. I., Larraondo, P. R., McVicar, T. R., Pan, M., Dutra, E., and Miralles, D. G.: MSWX: Global 3-hourly 0.1 bias-corrected meteorological data including near-real-time updates and forecast ensembles, Bulletin of the American Meteorological Society, 103, E710–E732, https://doi.org/https://doi.org/10.1175/BAMS-D-21-0145.1, 2022.

Beguería, S., Haro-Monteagudo, D., Palazón Tabuenca, L., and García-Ruiz, J. M.: Interacciones montaña-llanura frente al cambio global: desafíos y oportunidades en la gestión del territorio y de los recursos hídricos en Riegos del Alto Aragón, https://doi.org/https://doi.org/10.3989/pirineos.2022.177005, 2022.

Beguería, S., Trullenque-Blanco, V., Vicente-Serrano, S. M., and González-Hidalgo, J. C.: Aridity on the Rise: Spatial and Temporal Shifts in Climate Aridity in Spain (1961–2020), International Journal of Climatology, 45, e8775, https://doi.org/https://doi.org/10.1002/joc.8775, 2025.

Boone, A., Bellvert, J., Best, M., Brooke, J. K., Canut-Rocafort, G., Cuxart, J., Hartogensis, O., Le Moigne, P., Miró, J. R., Polcher, J., et al.: The land surface interactions with the atmosphere over the iberian semi-arid environment (LIAISE) field campaign, Journal of the European Meteorological Society, 2, 100 007, https://doi.org/https://doi.org/10.1016/j.jemets.2025.100007, 2025.

Bossard, M., Feranec, J., Otahel, J., et al.: CORINE land cover technical guide: Addendum 2000, vol. 40, European Environment Agency Copenhagen, 2000.

Carrer, D., Ceamanos, X., Moparthy, S., Vincent, C., C. Freitas, S., and Trigo, I. F.: Satellite retrieval of downwelling shortwave surface flux and diffuse fraction under all sky conditions in the framework of the LSA SAF program (Part 1: Methodology), Remote Sensing, 11, 2532, https://doi.org/https://doi.org/10.3390/rs11212532, 2019.

Carvalho, D., Cardoso Pereira, S., and Rocha, A.: Future surface temperature changes for the Iberian Peninsula according to EURO-CORDEX climate projections, Climate Dynamics, 56, 123–138, https://doi.org/https://doi.org/10.1007/s00382-020-05472-3, 2021.

Chen, T. and Guestrin, C.: Xgboost: A scalable tree boosting system, in: Proceedings of the 22nd acm sigkdd international conference on knowledge discovery and data mining, pp. 785–794, https://doi.org/https://doi.org/10.1145/2939672.2939785, 2016.

https://doi.org/10.5194/egusphere-2026-1856
Preprint. Discussion started: 10 April 2026

Cruz Maceín, J. L., Gonzalez-Fernandez, I., Barrutieta, A., Bermejo-Bermejo, V., and Zamorano Rodríguez, J. P.: Adaptation strategies for dealing with global atmospheric change in Mediterranean agriculture: a triple helix approach to the Spanish case study, Regional Environmental Change, 23, 142, https://doi.org/https://doi.org/10.1007/s10113-023-02131-1, 2023.

Dari, J., Brocca, L., Quintana-Seguí, P., Escorihuela, M. J., Stefan, V., and Morbidelli, R.: Exploiting high-resolution remote sensing soil moisture to estimate irrigation water amounts over a Mediterranean region, Remote Sensing, 12, 2593, https://doi.org/https://doi.org/10.3390/rs12162593, 2020.

Dari, J., Brocca, L., Modanesi, S., Massari, C., Tarpanelli, A., Barbetta, S., Quast, R., Vreugdenhil, M., Freeman, V., Barella-Ortiz, A., Quintana-Seguí, P., Bretreger, D., and Volden, E.: Regional data sets of high-resolution (1 and 6 km) irrigation estimates from space, Earth System Science Data, 15, 1555–1575, https://doi.org/10.5194/essd-15-1555-2023, 2023.

Dari, J., Filippucci, P., and Brocca, L.: The development of an operational system for estimating irrigation water use reveals socio-political dynamics in Ukraine, Hydrology and Earth System Sciences, 28, 2651–2659, https://doi.org/https://doi.org/10.5194/hess-28-2651-2024, 2024a.

Dari, J., Quintana-Seguí, P., Barella-Ortiz, A., Rahmati, M., Saltalippi, C., Flammini, A., and Brocca, L.: Quantifying the hydrological impacts of irrigation on a Mediterranean agricultural context through explicit satellite-derived irrigation estimates, Water Resources Research, 60, e2023WR036 510, https://doi.org/https://doi.org/10.1029/2023WR036510, 2024b.

DiMiceli, C., Sohlberg, R., and Townshend, J.: MODIS/Terra Vegetation Continuous Fields Yearly L3 Global 250m SIN Grid V061 [Data set], https://doi.org/https://doi.org/10.5067/MODIS/MOD44B.061, 2022.

Domingo, R. and Castel, J.: Review. Deficit irrigation in fruit trees and vines in Spain, Spanish Journal of Agricultural Research, 8, 5–20, https://doi.org/https://doi.org/10.5424/sjar/201008S2-1343, 2010.

Duarte, R., Pinilla, V., and Serrano, A.: The water footprint of the Spanish agricultural sector: 1860–2010, Ecological Economics, 108, 200–207, https://doi.org/http://dx.doi.org/10.1016/j.ecolecon.2014.10.020, 2014.

Endsley, K. A., Zhao, M., Kimball, J. S., Albrethsen, T., and Devadiga, S.: Improved global estimates of terrestrial evapotranspiration using the MODIS and VIIRS sensors, Journal of Hydrometeorology, 26, 817–833, 2025.

Ermida, S. L., Trigo, I. F., DaCamara, C. C., and Pires, A. C.: A methodology to simulate LST directional effects based on parametric models and landscape properties, Remote Sensing, 10, 1114, https://doi.org/https://doi.org/10.3390/rs10071114, 2018.

Expósito, A. and Berbel, J.: Sustainability implications of deficit irrigation in a mature water economy: A case study in southern Spain, Sustainability, 9, 1144, https://doi.org/https://doi.org/10.3390/su9071144, 2017.

Fan, D., Zhao, T., Jiang, X., García-García, A., Schmidt, T., Samaniego, L., Attinger, S., Wu, H., Jiang, Y., Shi, J., et al.: A Sentinel-1 SAR-based global 1-km resolution soil moisture data product: Algorithm and preliminary assessment, Remote Sensing of Environment, 318, 114 579, https://doi.org/https://doi.org/10.1016/j.rse.2024.114579, 2025.

FAO: Agricultural Stress Index System (ASIS), http://www.fao.org/giews/earthobservation/, [Last accessed: October 7th, 2025], 2018.

FAO: WaPOR V2 Database Methodology. Remote Sensing for Water Productivity Technical Report: Methodology Series, Rome, FAO, https://doi.org/https://www.fao.org/3/ca9894en/CA9894EN.pdf, 2020.

Filippucci, P., Brocca, L., Ciabatta, L., Mosaffa, H., Avanzi, F., and Massari, C.: Development of HYPER-P: HYdroclimatic PERformance-enhanced Precipitation at 1 km/daily over the Europe-Mediterranean region from 2007 to 2022, Earth System Science Data, 17, 5221–5258, https://doi.org/https://doi.org/10.5194/essd-17-5221-2025, 2025.

https://doi.org/10.5194/egusphere-2026-1856
Preprint. Discussion started: 10 April 2026

Fisher, J. B., Tu, K. P., and Baldocchi, D. D.: Global estimates of the land–atmosphere water flux based on monthly AVHRR and ISLSCP-II data, validated at 16 FLUXNET sites, Remote Sensing of Environment, 112, 901–919, https://doi.org/https://doi.org/10.1016/j.rse.2007.06.025, 2008.

Fisher, J. B., Melton, F., Middleton, E., Hain, C., Anderson, M., Allen, R., McCabe, M. F., Hook, S., Baldocchi, D., Townsend, P. A., et al.: The future of evapotranspiration: Global requirements for ecosystem functioning, carbon and climate feedbacks, agricultural management, and water resources, Water resources research, 53, 2618–2626, https://doi.org/https://doi.org/10.1002/2016WR020175, 2017.

Funes, I., Savé, R., De Herralde, F., Biel, C., Pla, E., Pascual, D., Zabalza, J., Cantos, G., Borràs, G., Vayreda, J., et al.: Modeling impacts of climate change on the water needs and growing cycle of crops in three Mediterranean basins, Agricultural Water Management, 249, 106 797, https://doi.org/https://doi.org/10.1016/j.agwat.2021.106797, 2021.

García-Valdecasas Ojeda, M., Romero-Jiménez, E., Rosa-Cánovas, J. J., Yeste, P., Castro-Díez, Y., Esteban-Parra, M. J., Vicente-Serrano, S. M., and Gámiz-Fortis, S. R.: Assessing future drought conditions over the Iberian Peninsula: the impact of using different periods to compute the SPEI, Atmosphere, 12, 980, 2021.

Garrido-Perez, J. M., Vicente-Serrano, S. M., Barriopedro, D., Garcia-Herrera, R., Trigo, R., and Begueria, S.: Examining the outstanding Euro-Mediterranean drought of 2021–2022 and its historical context, Journal of Hydrology, 630, 130 653, https://doi.org/https://doi.org/10.1016/j.jhydrol.2024.130653, 2024.

Gebrechorkos, S. H., Sheffield, J., Vicente-Serrano, S. M., Funk, C., Miralles, D. G., Peng, J., Dyer, E., Talib, J., Beck, H. E., Singer, M. B., et al.: Warming accelerates global drought severity, Nature, pp. 1–8, https://doi.org/https://doi.org/10.1038/s41586-025-09047-2, 2025.

Gong, Z., Gao, F., Chang, X., Hu, T., and Li, Y.: A review of interactions between irrigation and evapotranspiration, Ecological Indicators, 169, 112 870, https://doi.org/https://doi.org/10.1016/j.ecolind.2024.112870, 2024.

Guerschman, J. P., McVicar, T. R., Vleeshower, J., Van Niel, T. G., Peña-Arancibia, J. L., and Chen, Y.: Estimating actual evapotranspiration at field-to-continent scales by calibrating the CMRSET algorithm with MODIS, VIIRS, Landsat and Sentinel-2 data, Journal of Hydrology, 605, 127 318, https://doi.org/https://doi.org/10.1016/j.jhydrol.2021.127318, 2022.

Gupta, H. V., Kling, H., Yilmaz, K. K., and Martinez, G. F.: Decomposition of the mean squared error and NSE performance criteria: Implications for improving hydrological modelling, Journal of hydrology, 377, 80–91, https://doi.org/https://doi.org/10.1016/j.jhydrol.2009.08.003, 2009.

Han, S., Tang, Q., Xu, D., and Wang, S.: Irrigation-induced changes in potential evaporation: more attention is needed., Hydrological Processes, 28, https://doi.org/https://doi.org/10.1002/hyp.10108, 2014.

Hersbach, H., Bell, B., Berrisford, P., Hirahara, S., Horányi, A., Muñoz-Sabater, J., Nicolas, J., Peubey, C., Radu, R., Schepers, D., et al.: The ERA5 global reanalysis, Quarterly journal of the royal meteorological society, 146, 1999–2049, https://doi.org/https://doi.org/10.1002/qj.3803, 2020.

Hulsman, P., Keune, J., Koppa, A., Schellekens, J., and Miralles, D. G.: Incorporating plant access to groundwater in existing global, satellite-based evaporation estimates, Water Resources Research, 59, https://doi.org/https://doi.org/10.1029/2022WR033731, 2023.

Ilvonen, L., López-Sáez, J. A., Holmström, L., Alba-Sánchez, F., Pérez-Díaz, S., Carrión, J. S., Ramos-Román, M. J., Camuera, J., Jiménez-Moreno, G., Ruha, L., et al.: Spatial and temporal patterns of Holocene precipitation change in the Iberian Peninsula, Boreas, 51, 776–792, https://doi.org/https://doi.org/10.1111/bor.12586, 2022.

Inness, A., Ades, M., Agustí-Panareda, A., Barré, J., Benedictow, A., Blechschmidt, A.-M., Dominguez, J. J., Engelen, R., Eskes, H., Flemming, J., et al.: The CAMS reanalysis of atmospheric composition, Atmospheric Chemistry and Physics, 19, 3515–3556, https://doi.org/https://doi.org/10.5194/acp-19-3515-2019, 2019.

https://doi.org/10.5194/egusphere-2026-1856
Preprint. Discussion started: 10 April 2026

Jagadish, S. K., Way, D. A., and Sharkey, T. D.: Plant heat stress: Concepts directing future research, Plant, cell & environment, 44, 1992–2005, https://doi.org/https://doi.org/10.1111/pce.14050, 2021.

Jézéquel, A., Faranda, D., Drobinski, P., and Lionello, P.: Extreme Event Attribution in the Mediterranean, International Journal of Climatology, p. e8799, 2025.

Julia, C. and Dingkuhn, M.: Predicting temperature induced sterility of rice spikelets requires simulation of crop-generated microclimate, European Journal of Agronomy, 49, 50–60, https://doi.org/https://doi.org/10.1016/j.eja.2013.03.006, 2013.

Jung, M., Reichstein, M., and Bondeau, A.: Towards global empirical upscaling of FLUXNET eddy covariance observations: validation of a model tree ensemble approach using a biosphere model, Biogeosciences, 6, 2001–2013, https://doi.org/https://doi.org/10.5194/bg-6-2001-2009, 2009.

Junquera, V., Hormaza, J. I., Rubenstein, D. I., Levin, S. A., Vadillo Pérez, I., and Gavilán, P. J.: Severe water crisis in southern Spain under expanding irrigated agriculture: A multidimensional drought analysis, Proceedings of the National Academy of Sciences, 122, e2508055 122, https://doi.org/https://doi.org/10.1073/pnas.2508055122, 2025.

Kan, Y., Mu, X.-R., Gao, J., Lin, H.-X., and Lin, Y.: The molecular basis of heat stress responses in plants, Molecular Plant, 16, 1612–1634, https://doi.org/https://doi.org/10.1016/j.molp.2023.09.013, 2023.

Karger, D. N., Conrad, O., Böhner, J., Kawohl, T., Kreft, H., Soria-Auza, R. W., Zimmermann, N. E., Linder, H. P., and Kessler, M.: Climatologies at high resolution for the earth's land surface areas, Scientific data, 4, 1–20, https://doi.org/https://doi.org/10.1038/sdata.2017.122, 2017.

Kling, H., Fuchs, M., and Paulin, M.: Runoff conditions in the upper Danube basin under an ensemble of climate change scenarios, Journal of hydrology, 424, 264–277, https://doi.org/https://doi.org/10.1016/j.jhydrol.2012.01.011, 2012.

Koppa, A., Rains, D., Hulsman, P., Poyatos, R., and Miralles, D. G.: A deep learning-based hybrid model of global terrestrial evaporation, Nature Communications, 13, 1912, https://doi.org/https://doi.org/10.1038/s41467-022-29543-7, 2022.

Kustas, W. P., Norman, J. M., Schmugge, T. J., and Anderson, M. C.: Mapping surface energy fluxes with radiometric temperature, in: Thermal remote sensing in land surface processing, pp. 205–253, CRC Press, https://doi.org/https://doi.org/10.1201/9780203502174-c8, 2004.

Laluet, P., Corbari, C., Baez-Villanueva, O., Walther, S., Zhang, Y., Muñoz-Sabater, J., Senay, G. B., Albergel, C., and Dorigo, W.: Assessing the suitability of global evapotranspiration products over irrigated areas, EGUsphere, 2025, 1–29, https://doi.org/https://doi.org/10.5194/egusphere-2025-5716, 2025.

Laluet, P., Dari, J., Busschaert, L., Heyvaert, Z., De Lannoy, G., Langhans, P., Modanesi, S., Massari, C., Brocca, L., Saltalippi, C., et al.: Long-term irrigation water use datasets from multiple Earth Observation-based methods in major irrigated regions, Earth System Science Data Discussions, 2026, 1–30, https://doi.org/https://doi.org/10.5194/essd-2025-737, 2026.

Lambers, H. and Oliveira, R. S.: Plant energy budgets: The plant's energy balance, in: Plant physiological ecology, pp. 265–278, Springer, https://doi.org/https://doi.org/10.1007/978-3-030-29639-1_6, 2019.

Lazoglou, G., Papadopoulos-Zachos, A., Georgiades, P., Zittis, G., Velikou, K., Manios, E. M., and Anagnostopoulou, C.: Identification of climate change hotspots in the Mediterranean, Scientific reports, 14, 29 817, https://doi.org/https://doi.org/10.1038/s41598-024-80139-1, 2024.

Liu, Y., Zhuang, Q., Miralles, D., Pan, Z., Kicklighter, D., Zhu, Q., He, Y., Chen, J., Tchebakova, N., Sirin, A., et al.: Evapotranspiration in Northern Eurasia: Impact of forcing uncertainties on terrestrial ecosystem model estimates, Journal of Geophysical Research: Atmospheres, 120, 2647–2660, https://doi.org/https://doi.org/10.1002/2014JD022531, 2015.

https://doi.org/10.5194/egusphere-2026-1856
Preprint. Discussion started: 10 April 2026

Lorenzo, M., Pereira, H., Alvarez, I., and Dias, J.: Standardized Precipitation Index (SPI) evolution over the Iberian Peninsula during the 21st century, Atmospheric Research, 297, 107 132, https://doi.org/https://doi.org/10.1016/j.atmosres.2023.107132, 2024.

Luojus, K., Pulliainen, J., Takala, M., Lemmetyinen, J., Mortimer, C., Derksen, C., Mudryk, L., Moisander, M., Hiltunen, M., Smolander, T., et al.: GlobSnow v3. 0 Northern Hemisphere snow water equivalent dataset, Scientific Data, 8, 163, https://doi.org/https://doi.org/10.1038/s41597-021-00939-2, 2021.

Martens, B., Miralles, D. G., Lievens, H., Van Der Schalie, R., De Jeu, R. A., Fernández-Prieto, D., Beck, H. E., Dorigo, W. A., and Verhoest, N. E.: GLEAM v3: Satellite-based land evaporation and root-zone soil moisture, Geoscientific Model Development, 10, 1903–1925, https://doi.org/https://doi.org/10.5194/gmd-10-1903-2017, 2017.

Martens, B., De Jeu, R. A., Verhoest, N. E., Schuurmans, H., Kleijer, J., and Miralles, D. G.: Towards estimating land evaporation at field scales using GLEAM, Remote Sensing, 10, 1720, https://doi.org/https://doi.org/10.3390/rs10111720, 2018.

Maselli, F., Battista, P., Chiesi, M., Rapi, B., Angeli, L., Fibbi, L., Magno, R., and Gozzini, B.: Use of Sentinel-2 MSI data to monitor crop irrigation in Mediterranean areas, International Journal of Applied Earth Observation and Geoinformation, 93, 102 216, https://doi.org/https://doi.org/10.1016/j.jag.2020.102216, 2020.

Massari, C., Modanesi, S., Dari, J., Gruber, A., De Lannoy, G. J., Girotto, M., Quintana-Seguí, P., Le Page, M., Jarlan, L., Zribi, M., et al.: A review of irrigation information retrievals from space and their utility for users, Remote Sensing, 13, 4112, https://doi.org/https://doi.org/10.3390/rs13204112, 2021.

McCabe, M. F., Ershadi, A., Jimenez, C., Miralles, D. G., Michel, D., and Wood, E. F.: The GEWEX LandFlux project: Evaluation of model evaporation using tower-based and globally gridded forcing data, Geoscientific Model Development, 9, 283–305, https://doi.org/https://doi.org/10.5194/gmd-9-283-2016, 2016.

McDermid, S., Nocco, M., Lawston-Parker, P., Keune, J., Pokhrel, Y., Jain, M., Jägermeyr, J., Brocca, L., Massari, C., Jones, A. D., et al.: Irrigation in the Earth system, Nature Reviews Earth & Environment, 4, 435–453, https://doi.org/https://doi.org/10.1038/s43017-023-00438-5, 2023.

Meier, J., Zabel, F., and Mauser, W.: A global approach to estimate irrigated areas–a comparison between different data and statistics, Hydrology and Earth System Sciences, 22, 1119–1133, https://doi.org/https://doi.org/10.5194/hess-22-1119-2018, 2018.

Melton, F. S., Huntington, J., Grimm, R., Herring, J., Hall, M., Rollison, D., Erickson, T., Allen, R., Anderson, M., Fisher, J. B., et al.: OpenET: Filling a critical data gap in water management for the western United States, JAWRA Journal of the American Water Resources Association, 58, 971–994, https://doi.org/https://doi.org/10.1111/1752-1688.12956, 2022.

Miralles, D. G., Holmes, T. R. H., De Jeu, R. A. M., Gash, J. H., Meesters, A. G. C. A., and Dolman, A. J.: Global land-surface evaporation estimated from satellite-based observations, Hydrology and Earth System Sciences, 15, 453–469, https://doi.org/10.5194/hess-15-453-2011, 2011.

Miralles, D. G., Jiménez, C., Jung, M., Michel, D., Ershadi, A., McCabe, M., Hirschi, M., Martens, B., Dolman, A. J., Fisher, J. B., et al.: The WACMOS-ET project–Part 2: Evaluation of global terrestrial evaporation data sets, Hydrology and Earth System Sciences, 20, 823–842, https://doi.org/https://doi.org/10.5194/hess-20-823-2016, 2016.

Miralles, D. G., Bonte, O., Koppa, A., Villanueva, O. B., Tronquo, E., Zhong, F., Beck, H., Hulsman, P., Dorigo, W., Verhoest, N. E., et al.: GLEAM4: global land evaporation dataset at 0.1 resolution from 1980 to near present, Scientific Data, https://doi.org/https://doi.org/10.1038/s41597-025-04610-y, 2025.

https://doi.org/10.5194/egusphere-2026-1856
Preprint. Discussion started: 10 April 2026

Modanesi, S., Massari, C., Bechtold, M., Lievens, H., Tarpanelli, A., Brocca, L., Zappa, L., and De Lannoy, G. J. M.: Challenges and benefits of quantifying irrigation through the assimilation of Sentinel-1 backscatter observations into Noah-MP, Hydrology and Earth System Sciences, 26, 4685–4706, https://doi.org/10.5194/hess-26-4685-2022, 2022.

Modanesi, S., Busschaert, L., De Lannoy, G., De Santis, D., Natali, M., Dari, J., Quintana-Seguí, P., Castelli, M., Grasso, F. M., and Massari, C.: Accounting for scaling effects on irrigation optimization within a land surface model using satellite observations, Journal of Hydrometeorology, p. e250057, https://doi.org/https://doi.org/10.1175/JHM-D-25-0057.1, 2025.

Mu, Q., Zhao, M., and Running, S. W.: Improvements to a MODIS global terrestrial evapotranspiration algorithm, Remote sensing of environment, 115, 1781–1800, https://doi.org/https://doi.org/10.1016/j.rse.2011.02.019, 2011.

Myneni, R., Knyazikhin, Y., and Park, T.: MODIS/Terra+Aqua Leaf Area Index/FPAR 8-Day L4 Global 500m SIN Grid V061 [Data set], https://doi.org/https://doi.org/10.5067/MODIS/MCD15A2H.061, 2021.

Nelson, J. A., Walther, S., Gans, F., Kraft, B., Weber, U., Novick, K., Buchmann, N., Migliavacca, M., Wohlfahrt, G., Šigut, L., et al.: X-BASE: the first terrestrial carbon and water flux products from an extended data-driven scaling framework, FLUXCOM-X, Biogeosciences, 21, 5079–5115, https://doi.org/https://doi.org/10.5194/bg-21-5079-2024, 2024.

NOAA: ETOPO 2022 15 arc-second global relief model, https://doi.org/https://doi.org/10.25921/fd45-gt74, 2022.

Norman, J. M., asas, W. P., and Humes, K. S.: Source approach for estimating soil and vegetation energy fluxes in observations of directional radiometric surface temperature, Agricultural and Forest Meteorology, 77, 263–293, https://doi.org/https://doi.org/10.1016/0168-1923(95)02265-Y, 1995.

Ojeda, M. G.-V., Gámiz-Fortis, S. R., Romero-Jiménez, E., Rosa-Cánovas, J. J., Yeste, P., Castro-Díez, Y., and Esteban-Parra, M. J.: Projected changes in the Iberian Peninsula drought characteristics, Science of the Total Environment, 757, 143 702, https://doi.org/https://doi.org/10.1016/j.scitotenv.2020.143702, 2021.

OpenET: OpenET Data Explorer, https://etdata.org/openet-data-explorer/, accessed: 2026-03-13, 2026.

Pinilla, V.: The development of irrigated agriculture in twentieth-century Spain: a case study of the Ebro basin, Agricultural History Review, 54, 122–141, http://www.jstor.org/stable/40276057.Accessed30Mar.2026, 2006.

Playán, E., Gimeno, Y., Lorenzo-González, M., Jiménez, A., López-Pardo, J., Oliván, I., Castillo, R., Carbonell, X., Fábregas, M., Vicente, L., et al.: Irrigation modernization in the Ebro–Aragón region of Spain: Past and future trends, Agricultural Water Management, 302, 108 975, https://doi.org/https://doi.org/10.1016/j.agwat.2024.108975, 2024.

Potapov, P., Hansen, M. C., Pickens, A., Hernandez-Serna, A., Tyukavina, A., Turubanova, S., Zalles, V., Li, X., Khan, A., Stolle, F., et al.: The global 2000-2020 land cover and land use change dataset derived from the Landsat archive: first results, Frontiers in Remote Sensing, 3, 856 903, https://doi.org/https://doi.org/10.3389/frsen.2022.856903, 2022.

Purnamasari, D., Teuling, A. J., and Weerts, A. H.: Identifying irrigated areas using land surface temperature and hydrological modelling: application to the Rhine basin, Hydrology and Earth System Sciences, 29, 1483–1503, https://doi.org/https://doi.org/10.5194/hess-29-1483-2025, 2025.

Puy, A., Linga, S. N., Wei, N., Flinders, S., Callow, B., Allen, G., Cross, B., Aguiló-Rivera, C., and Lankford, B.: Widely cited global irrigation statistics lack empirical support, PNAS nexus, 4, pgaf323, https://doi.org/https://doi.org/10.1093/pnasnexus/pgaf323, 2025.

Rains, D., Trigo, I., Dutra, E., Ermida, S., Ghent, D., Hulsman, P., Gómez-Dans, J., and Miralles, D. G.: High-resolution (1 km) all-sky net radiation over Europe enabled by the merging of land surface temperature retrievals from geostationary and polar-orbiting satellites, Earth System Science Data, 16, 567–593, https://doi.org/https://doi.org/10.5194/essd-16-567-2024, 2024.

https://doi.org/10.5194/egusphere-2026-1856
Preprint. Discussion started: 10 April 2026

Scanlon, B. R., Fakhreddine, S., Rateb, A., de Graaf, I., Famiglietti, J., Gleeson, T., Grafton, R. Q., Jobbagy, E., Kebede, S., Kolusu, S. R., et al.: Global water resources and the role of groundwater in a resilient water future, Nature Reviews Earth & Environment, 4, 87–101, https://doi.org/https://doi.org/10.1038/s43017-022-00378-6, 2023.

Schaaf, C. and Wang, Z.: MODIS/Terra+Aqua BRDF/Albedo Quality Daily L3 Global - 500m V061 [Data set], https://doi.org/https://doi.org/10.5067/MODIS/MCD43A2.061, 2021.

Serrano-Notivoli, R., Beguería, S., Saz-Sánchez, M. Á., and Luis, M. d.: Recent trends reveal decreasing intensity of daily precipitation in Spain, International Journal of Climatology, https://doi.org/https://doi.org/10.1002/joc.5562, 2018.

Serrano-Notivoli, R., Tejedor, E., Sarricolea, P., Meseguer-Ruiz, O., de Luis, M., Saz, M. Á., Longares, L. A., and Olcina, J.: Unprecedented warmth: A look at Spain's exceptional summer of 2022, Atmospheric Research, 293, 106 931, https://doi.org/https://doi.org/10.1016/j.atmosres.2023.106931, 2023.

Siebert, S., Döll, P., Hoogeveen, J., Faures, J.-M., Frenken, K., and Feick, S.: Development and validation of the global map of irrigation areas, Hydrology and Earth System Sciences, 9, 535–547, https://doi.org/10.5194/hess-9-535-2005, 2005.

Simons, G., Koster, R., and Droogers, P.: Hihydrosoil v2. 0-high resolution soil maps of global hydraulic properties, Future Works.[online] Available from https://www. futurewater. eu/projects/hihydrosoil, 2020.

Spinoni, J., Barbosa, P., Bucchignani, E., Cassano, J., Cavazos, T., Christensen, J. H., Christensen, O. B., Coppola, E., Evans, J., Geyer, B., et al.: Future global meteorological drought hot spots: a study based on CORDEX data, Journal of Climate, 33, 3635–3661, https://doi.org/https://doi.org/10.1175/JCLI-D-19-0084.1, 2020.

Sutanto, S. J., Janssen, M., De Brito, M. M., and del Pozo Garcia, M.: The effect of wildfires on flood risk: a multi-hazard flood risk approach for the Ebro River basin, Spain, Natural Hazards and Earth System Sciences, 24, 3703–3721, https://doi.org/https://doi.org/10.5194/nhess-24-3703-2024, 2024.

Tedesco, M., Kelly, R., Foster, J., and Chang, A.: AMSR-E/Aqua Daily L3 Global Snow Water Equivalent EASE-Grids, Version 2, https://doi.org/10.5067/AMSR-E/AE_DYSNO.002, 2004.

Tocados-Franco, E., Berbel, J., and Expósito, A.: Water policy implications of perennial expansion in the Guadalquivir River Basin (southern Spain), Agricultural Water Management, 282, 108 286, https://doi.org/https://doi.org/10.1016/j.agwat.2023.108286, 2023.

Tran, B. N., Van Der Kwast, J., Seyoum, S., Uijlenhoet, R., Jewitt, G., and Mul, M.: Uncertainty assessment of satellite remote-sensing-based evapotranspiration estimates: a systematic review of methods and gaps, Hydrology and Earth System Sciences, 27, 4505–4528, 2023.

Trigo, I. F., Peres, L. F., DaCamara, C. C., and Freitas, S. C.: Thermal land surface emissivity retrieved from SEVIRI/Meteosat, IEEE Transactions on Geoscience and Remote Sensing, 46, 307–315, https://doi.org/https://doi.org/10.1109/TGRS.2007.905197, 2008.

Trigo, I. F., Dacamara, C. C., Viterbo, P., Roujean, J.-L., Olesen, F., Barroso, C., Camacho-de Coca, F., Carrer, D., Freitas, S. C., García-Haro, J., et al.: The satellite application facility for land surface analysis, International journal of remote sensing, 32, 2725–2744, https://doi.org/https://doi.org/10.1080/01431161003743199, 2011.

Van Dijk, A. I., Schellekens, J., Yebra, M., Beck, H. E., Renzullo, L. J., Weerts, A., and Donchyts, G.: Global 5 km resolution estimates of secondary evaporation including irrigation through satellite data assimilation, Hydrology and Earth System Sciences, 22, 4959–4980, https://doi.org/https://doi.org/10.5194/hess-22-4959-2018, 2018.

van Dijk, A. I. J. M. and Bruijnzeel, L. A.: Modelling rainfall interception by vegetation of variable density using an adapted analytical model. Part 1. Model description, Journal of Hydrology, 247, 230–238, https://doi.org/https://doi.org/10.1016/s0022-1694(01)00392-4, 2001.

https://doi.org/10.5194/egusphere-2026-1856
Preprint. Discussion started: 10 April 2026

Wagner, W., Lindorfer, R., Melzer, T., Hahn, S., Bauer-Marschallinger, B., Morrison, K., Calvet, J.-C., Hobbs, S., Quast, R., Greimeister-Pfeil, I., et al.: Widespread occurrence of anomalous C-band backscatter signals in arid environments caused by subsurface scattering, Remote Sensing of Environment, 276, 113 025, https://doi.org/https://doi.org/10.1016/j.rse.2022.113025, 2022.

Wan, Z., Hook, S., and Hulley, G.: MODIS/Terra Land Surface Temperature/Emissivity Daily L3 Global 1km SIN Grid V061 [Data set], https://doi.org/https://doi.org/10.5067/MODIS/MOD11A1.061, 2021.

Yi, K., Senay, G. B., Fisher, J. B., Wang, L., Suvočarev, K., Chu, H., Moore, G. W., Novick, K. A., Barnes, M. L., Keenan, T. F., et al.: Challenges and future directions in quantifying terrestrial evapotranspiration, Water Resources Research, 60, e2024WR037 622, https://doi.org/https://doi.org/10.1029/2024WR037622, 2024.

Zappa, L., Dari, J., Modanesi, S., Quast, R., Brocca, L., De Lannoy, G., Massari, C., Quintana-Seguí, P., Barella-Ortiz, A., and Dorigo, W.: Benefits and pitfalls of irrigation timing and water amounts derived from satellite soil moisture, Agricultural Water Management, 295, 108 773, https://doi.org/https://doi.org/10.1016/j.agwat.2024.108773, 2024.

Zhang, Y., Kong, D., Gan, R., Chiew, F. H., McVicar, T. R., Zhang, Q., and Yang, Y.: Coupled estimation of 500 m and 8-day resolution global evapotranspiration and gross primary production in 2002–2017, Remote sensing of environment, 222, 165–182, https://doi.org/https://doi.org/10.1016/j.rse.2018.12.031, 2019.

Zhao, M., A, G., Liu, Y., and Konings, A. G.: Evapotranspiration frequently increases during droughts, Nature Climate Change, 12, 1024–1030, https://doi.org/https://doi.org/10.1038/s41558-022-01505-3, 2022.

Zhong, F., Jiang, S., Dijk, A. I. J. M. v., Ren, L., Schellekens, J., and Miralles, D. G.: Revisiting large-scale interception patterns constrained by a synthesis of global experimental data, Hydrology and Earth System Sciences, 26, 5647–5667, https://doi.org/https://doi.org/10.5194/hess-26-5647-2022, 2022.

Zhong, F., Jiang, S., Koppa, A., Ren, L., Liu, Y., Wang, M., and Miralles, D. G.: Multi-Decadal Dynamics of Global Rainfall Interception and Their Drivers, Geophysical Research Letters, 51, https://doi.org/https://doi.org/10.1029/2024gl109295, 2024.

Zhu, W., Baumert, J., Storm, H., Heckelei, T., and Siebert, S.: ECIRA-European crop-specific irrigated area at 1 km resolution annually from 2010 to 2020, Scientific Data, 12, 1349, https://doi.org/https://doi.org/10.1038/s41597-025-05628-y, 2025.

Zotta, R.-M., Moesinger, L., Van Der Schalie, R., Vreugdenhil, M., Preimesberger, W., Frederikse, T., De Jeu, R., and Dorigo, W.: VODCA v2: multi-sensor, multi-frequency vegetation optical depth data for long-term canopy dynamics and biomass monitoring, Earth System Science Data, 16, 4573–4617, https://doi.org/https://doi.org/10.5194/essd-16-4573-2024, 2024.